

Measurement of Mass Evaporation of Ni-Based Single Crystal Super Alloy Using Electrostatic Levitation (ESL) & Electromagnetic Levitation (EML)

Submitted By
Jannatun Nawer

IN PARTIAL FULFILLMENT OF THE REQUIREMENTS FOR THE DEGREE OF
MASTER OF SCIENCE IN MECHANICAL ENGINEERING

School of Engineering
Tufts University
Medford, Massachusetts

May 2018



Signature of Author:
Jannatun Nawer



Certified By:
Associate Professor Douglas M. Matson
Department of Mechanical Engineering
Tufts University



Committee:
Assistant Professor Robert Peattie
Department of Surgery
Tufts Medical Center



Committee:
Assistant Professor Iryna Zenyuk
Department of Mechanical Engineering
Tufts University

Abstract

Increasing usage of Nickel-based super alloys in aerospace, power plant and nuclear reactors has made it necessary to model fluid flow during casting process. It is crucial to measure thermo-physical properties of these alloys accurately for this modelling purpose. Ni-based single crystal super alloy CMSX-4 plus were investigated for mass evaporation to analyze the mass loss using Electro Static Levitation (ESL) method. Two models were developed to predict the mass loss & dynamic mass during each thermal cycle. The first model predicts the rate of mass evaporation in ideal case where the evaporation is maximum with a correction factor. The second model predicts the mass evaporation with a correction of Aluminum activity which was calculated by evaluating the results from elemental analysis for Al, Cr, Ti, and Co. Both the models were applied and compared with the data obtained from another super alloy CMSX-10K using ESL. The models were also applied to CMSX-10K processed in Electro Magnetic Levitation (EML) to compare its accuracy for different sample size. Both models are not viable for analyzing space data yielding significant error. The 2nd model predicts the mass evaporation for Al & Co within ± 6 % errors for CMSX-4 plus samples processed in ESL.

Acknowledgements

I have been extremely fortunate to have had the support of the department, family, friends and colleagues. Without this support, this thesis would not have been possible.

First, I would like to thank my adviser, Dr. Douglas Matson for supporting me with my academic goals and for encouraging my research. Without his helpful suggestions, comments and constructive criticism this thesis would not have been completed. I am grateful for his constant effort on helping me push my boundaries and grow as a researcher.

I would like to acknowledge the financial support for this research work provided by NASA through the “Round Robin” grant NNX17AH41G. Special thanks to NASA Marshal Space Flight Centre Electro Static Levitator Team including Michael SanSoucie, Trudy Allen, and Glenn Fountain. I would also like to thank Ken Harris from Canon Muskegon for providing us with necessary raw material for our experiment.

I am thankful to my family for their undivided faith in me. Your endless support and encouragement helped me become who I am today. for always being there for me. Most importantly, I would like to thank my closest confidant, Ratul for being my constant support system and an awesome companion.

Next, I would like to thank many wonderful friends who helped me survive grad school. Thanks to Jessica who has helped me survive through the last two years with her constant support and wonderful friendship. I would also like to thank my friend and roommate Prajakta for all the foods and times we have shared. Thanks to lab group for keeping me company during writing this thesis and answering all of my questions. Special thanks to Pat, without whom this journey would have been impossible. I would also like to thank Forum, Kim and Raymond for all their support and kindness.

Table of Contents

1	Introduction	1
2	Background	3
2.1	Levitation Techniques	4
2.2	Alloy Selection	6
3	Methodology	11
3.1	Sample preparation	11
3.2	Experimental Apparatus for ESL	17
3.3	Experimental Procedure for ESL	18
3.4	Electromagnetic Levitation (EML)	19
3.5	Mass Evaporation of Super Alloys	20
4	Experimental Results	27
4.1	Prediction of Mass Evaporation in Ideal Case	30
4.2	Elemental Analysis	39
4.3	Prediction of Mass Evaporation with Corrected Al Activity	40
5	Modelling Comparison	44
6	Discussion	46
7	Conclusions	48
8	Future Work	50
9	References	51

List of Tables

Table I: Nominal compositions of SX alloys provided by Canon Muskegon	6
Table II: Room Temperature density of commercial alloys	7
Table III: List of Important properties of relevant elements	8
Table IV: AWJ cutting parameters used in machining the sample	13
Table V: List of Properties of DWH 4122 Diamond Wheel in NASA MSFC	15
Table VI: Vapor pressure polynomial equation coefficients for individual element	25
Table VII: Data obtained from ESL testing in NASA MSFC for CMSX-4 Plus	27
Table VIII: Comparison of reference & observed temperature	28
Table IX: Data analysis for Model 1	38
Table X: Result from elemental analysis of CMSX-4 plus samples	39
Table XI: Data analysis for Model 2	43
Table XII: Correction Factor & relative error for Three different samples	44
Table XIII: Comparison of models for CMSX-4 Plus	45

List of Figures

Figure 1: Sample levitated in EML	4
Figure 2: Sample levitated in ESL	5
Figure 3: Performance comparison with alloy development	9
Figure 4: Raw material provided by Canon Muskegon	11
Figure 5: Abrasive Water Jet Cutter in action in NASA MSFC machine shop	12
Figure 6: A diagram of the planned cutting path of the sample	14
Figure 7 : Sample rod obtained from AWJ Processing	14
Figure 8 : Diamond Wheel Cutting tool in NASA MSFC ESL facility	15
Figure 9: Electric Arc Melt furnace at NASA MSFC ESL facility	16
Figure 10: Schematic of the Electro Static Levitator at NASA MSFC	17
Figure 11: The ESL setup at NASA MSFC	18
Figure 12: (a) A levitated sample in ESL and (b) a sample observed during density analysis	19
Figure 13: EML SUPOS coil used in positioning and heating sample on the ISS	20
Figure 14: A single melt cycle of one of the CMSX-10 sample	20
Figure 15: Corrected Time Temperature profile of a CMSX-10K Sample	28
Figure 16: Measured vapor pressure for different element processed in ESL	29
Figure 17: Density of CMSX-10K as a function temperature	30
Figure 18: Density of CMSX-4 plus as a function temperature	30
Figure 19: Time-Temperature-Mass profile of a CMSX-4 plus sample MAT 1256	31
Figure 20: Evaporation comparison of elements of MAT 1256	33
Figure 21: Time Temperature Mass profile of a sample MAT 1257	33
Figure 22: Evaporation comparison of elements of MAT 1257	34
Figure 23: Time-Temperature-Mass profile of a CMS-10K sample MAT 867	35
Figure 24: Evaporation comparison of elements of sample 867	35
Figure 25: Time temperature profile of a CMSX-10K sample MAT 868	36
Figure 26: Evaporation comparison of elements of sample 868	36
Figure 27: A typical melt cycle of a CMSX-10K sample processed in EML	37
Figure 28: Ratio of compositions of EML sample	37
Figure 29: Time Temperature mass profile for MAT 1256 for no Al evaporation	40
Figure 30: Comparison of compositions while no Al is evaporated in MAT 1256	40
Figure 31: Time temperature mass profile for MAT 1257 for no Al evaporation	41
Figure 32: Comparison of compositions while no Al is evaporated in MAT 1257	41
Figure 33: Time temperature mass profile for MAT 867	42
Figure 34: Comparison of compositions while no Al is evaporated in MAT 867	42

Nomenclature

A	Area of the sample [mm^2]
a	Activity of individual substance
c	Mass fraction
g	Mass of an element [m/s^2]
I	Intensity of the laser
L	Length of the sample levitated
M	Molecular Mass of an element
m	Mass of an element [mg]
n	Number of components
\dot{m}	Rate of mass evaporation of an element [mg]
V	Potential difference [Volt]
Q	Magnitude of charges [C]
P_v	Vapor Pressure [Pa]
P_{ref}	Reference Pressure [Pa]
R	Universal Gas Constant [J/kg.mole]
T	Absolute Temperature [K]
α	Correction Factor
ε	Emissivity
σ	Boltzmann Constant
ρ	Density of the sample [kg/m^3]
γ	Activity coefficient
λ	Wavelength [m]

1 Introduction

The study of turbulent, transient fluid flow of molten metal through a complex geometry into a mold cavity during casting process is of great interest because of its influence on the quality of the product. It is very important to understand the heat transfer to the shell during initial stages of solidification and nucleation process. Extensive work has been done in the past to successfully investigate the fluid flow of continuous casting process in the mold region [1][2][3][4][5][6].

Recent technological development has made it possible to visualize the fluid flow, melt convection and heat flux distribution to accurately predict the evolution of microstructures. This evolution of microstructure is important in manufacturing products to achieve desired properties. The key to predict accurate models is to measure the thermo-physical properties during a melt cycle which can be challenging because of high fluidity and reactivity of molten metals. Thus, to develop physical models to describe phase selection and evolution of solidification structures, the quality of thermo-physical properties needs to be improved. Density, volume expansion, constant pressure heat capacity, total hemispherical emissivity, surface tension and viscosity are the properties of interest of many research groups [7] [8] [9] [10] [11] [12] [13] [14].

During casting process, the material is first heated to melt completely and then poured into the cavity of the mold. The material needs to be remain melted till it fills the mold cavity. Before the solidification process starts the material is exposed to a temperature higher than its melting temperature. In between this time, the volatile component of the alloy system starts to evaporate. To model fluid flow during casting, it is important to know how much mass we are losing during the melting and solidification, which component of the element we are losing, and in which order we are losing components and how long does it take to lose any particular component. In a nutshell, we can calculate how long our testing process is viable.

The main aim of this research is to build a model which can be used to calculate mass evaporation for any complex system of alloy. Since it is difficult to simulate casting with a large component, this model is developed using small sample of Nickel based super alloy using container-less processing. So, this research was conducted to find the answer to the following key questions:

1. Is it possible to predict mass evaporation as a function of temperature during each thermal cycle?
2. Which volatile element of the alloy system is evaporating and in what order?
3. How long the testing is viable i.e. how long does it take to lose one element from the alloy?

2 Background

The European Space Agency (ESA) assembled International Topical teams to investigate key topics specific to material science. The team led by Hans Fecht concentrated on addressing evaluation of thermo-physical properties at high temperature melt. The International Topical team led by Dieter Herlach focused on how melt convection influences different microstructure formation of alloys. The first team focused on ground and space-based investigations to develop prediction models of evaluating thermos-physical properties. The National Aeronautics and Space Administration (NASA) sponsored two projects LOADSTARS and ELFSTONE to aid these two team efforts [15]. Thermolab-ISS topical team collaborated on LOADSTARS (Levitation Observation of Dendrite Evaluation in Steel Ternary Alloy Rapid Solidification) project emphasized on improving the microstructural evaluation. The ELFSTONE (Electromagnetic Levitation Flight Support for Transient Observation of Nucleation Events), led by Thomas Volkman and Douglas Matson to observe convection in phase selection. Round Robin project was initiated to support this modelling processes. To conduct these prediction modelling activities accurately, the key thermophysical properties needs to be known as a function of temperature.

It is very important to address the problems of alloy freckle formation and grain growth encountered in solidification process, and to eliminate these problems it is crucial to measure accurate values of density along with its temperature dependency. Accuracy of viscosity and surface tension measurement greatly depend on accuracy of density. Several techniques have traditionally been used to study thermo-physical properties at high temperature melt. Among these are sessile drop [16], pycnometer [17], dilatometry Archimedean [18], maximum bubble pressure method [19] and levitation techniques [20].

2.1 Levitation Techniques

Non-contacting or container less processing has been an effective tool in the study of undercooling metallic melts which eliminates the possibility of heterogeneous nucleation on container wall, container induced contamination and restricts deformation. Sample is levitated using non-contacting forces such as electrostatic force, electromagnetic force and gas pressure from an airstream or acoustic fields. Due to absence of hydrostatic pressure in microgravity, the sample liquid is confined by their own surface tension which offers the possibility of melting and solidifying the sample without any physical contact. Electromagnetic levitation (EML) and electrostatic levitation (ESL) are two widely used levitation techniques.

EML offers a processing of electrically conductive metals, alloys and semi-conductors. Typical EML sample are of 5 to 8 mm in diameter. EML levitates the sample using Lorentz forces generated by alternating currents running through water cooled Copper coils. The sample is placed in the center of a coil system and the sample is heated by inducing eddy currents in the sample as shown in Figure 1.

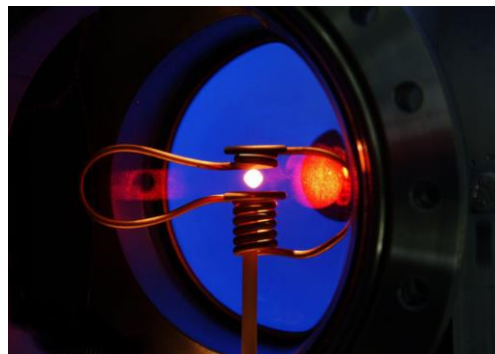


Figure 1: Sample levitated in EML (Photo Courtesy NASA)

The sample is kept in the center by creating a displacement field through the interaction of eddy current and the electromagnetic field. The heating and positioning of the sample is dependent on each other as the sample starts heating up just by applying the displacement field. So, the

undercooled region of samples with low melting is not accessible with this method. To counteract gravity, a huge amount of electromagnetic force is required which induces electromagnetic pressure on the sample resulting in strong convection. The liquid samples get deformed into an obolid shape which must be considered while measuring volume of the sample. The dynamic mass and volume can be tracked throughout the process. The EML samples are processed in atmospheric pressure so the mass evaporation is almost negligible. D. M. Matson et al. has briefly described the EML testing on the International Space Station (ISS) in a research article published in 2016 [21].

The ESL method uses Coulomb force to cancel the gravity between the sample and the surrounding electrodes. The force-balance equation [22] for the levitation of the sample is approximately given by equation (1).

$$mg = \frac{qV}{L} \quad (1)$$

Where, m is mass, g is gravitational acceleration, Q is the amount of charges transferred, V is the voltage required and L is the length of the sample. Figure 2 shows a levitated ESL sample.

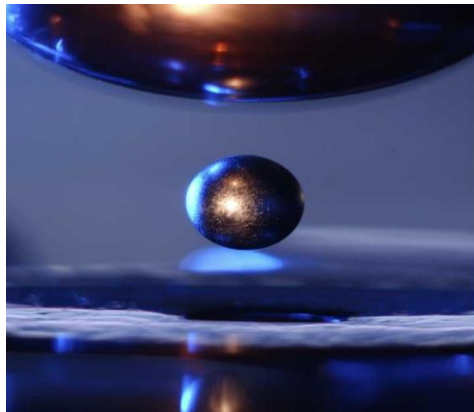


Figure 2: Sample levitated in ESL (Photo courtesy NASA)

ESL samples are smaller compared to EML samples. They are typically within 2 to 3 mm in diameter. ESL has several advantages over EML. ESL is not limited to conductive material as

EML. The ESL samples have minimal deviation from the spherical shape in the liquid form due to smaller sample size. ESL sample needs to be processed in vacuum to avoid electric arcing which increases the rate of mass evaporation. Therefore, it is crucial to measure density as a function of temperature.

2.2 Alloy Selection

A large part of aero and ground-based gas turbine engine blades is made using directional solidification process. This controlled solidification technique has been used to produce both columnar grain and alloy single crystal gas turbine blade [23]. Alloys with good stability and lower crack-growth rates are desired for lower component costs, lower life-cycle costs and lower maintenance costs. Turbine blades withstand very high pressure and high temperature which requires very specialized materials. Nickel based super alloys offers an exceptional combination of high temperature strength, higher creep resistance, toughness and resistance to corrosion [24] [25] [26]. Turbine blades are mostly casted as equiaxed grains or single crystal without no grain boundaries so the possibilities of damage at high temperature is significantly reduced [27]. A good number of series of Nickel based alloys has been developed along with other refractory alloying elements such as Cr, Co, Mo, W, Al, Ti, Ta and sometimes Nb or V [28].

Table I: Nominal compositions of SX alloys provided by Canon Muskegon

Alloy	Cr	Co	Mo	Ta	W	Nb	Re	Al	Ti	Hf	Ni
CMSX-4	6.5	9.6	0.6	6.5	6.4	-	3	5.6	1	0.1	Bal
CMSX-4 Plus	3.5	10	0.6	8	6	0.1	4.8	5.69	0.85	0.1	Bal
CMSX-10K	2	3	0.4	8	5	0.1	6	5.6	0.2	0.03	Bal

For this experiment we have worked with two Ni based superalloys CMSX-10K and CMSX-4 Plus. CMSX-10K is a third-generation super alloy which is used in uncooled 2nd stages of blades containing 6-7% pf Re [29]. CMSX-4 Plus is an improved third-generation super alloy with lower Re content and superior high temperature mechanical properties. It is a development of CMSX-4 to achieve properties of CMSX-10K but with lower density.

A comparison of chemical compositions of some relevant alloys with the experimental alloys is shown in table 1. Re content has been increased for both the alloys for improved creep ruptured properties. High Ta content improves cast ability with no freckling. Cr content has been adjusted for increased phase stability and Ti has been adjusted for interfacial chemistry. High content of Al combined with low content of Mo provides improved bare alloy oxidation (coating adherence).

CMSX- 4 plus has better single crystal (SX) cast ability, high oxidation resistance and better creep rupture properties compared to CMSX-10. A comparison of density of CMSX-10K and CMSX-4 plus with other commercial alloys are shown in Table I.

Table II: Room Temperature density of commercial alloys [30]

Alloy	Room Temperature Density (g/cm^3)
AM1	8.59
CMSX-4	8.70
SC 180	8.84
CMSX-4 Plus	8.93
PWA 1484	8.95
Rene N6	8.97
CMSX-10K	9.05

CMSX-4 Plus has a density of 8.92 g/cm³ which is lower than CSMX-10K. Zushu Li et. al measured density & surface tension of various Ni-based super alloys in both mushy & liquid states using MSDM & MPM in 2005[31]. The authors correlated density (ρ) of CMSX-10K with temperature (T) with equations (2) & (3) based on experimental results which gives density within 6% errors.

$$\text{Liquid, } \rho \text{ (kg/m}^3\text{)}=8080-0.661 \times (T-1676 \text{ K}) \quad (2)$$

$$\text{Mushy, } \rho \text{ (kg/m}^3\text{)}=8170-2.96 \times (T-1644 \text{ K}) \quad (3)$$

In another article, E. Ricci measured density of CMSX-4 using sessile drop method and developed a theoretical relationship between density & temperature in equations (4) & (5) which gives density with a deviation less than 1.5% [32].

$$\text{Liquid, } \rho \text{ (kg/m}^3\text{)}=7781-0.41 \times (T-1654 \text{ K}) \quad (4)$$

$$\text{Mushy, } \rho \text{ (kg/m}^3\text{)}=7880-1.32 \times (T-1644 \text{ K}) \quad (5)$$

A list of important properties of the elements of CMSX-10K and CMSX-4 Plus is listed in Table III which were used later during the calculation of mass evaporation.

Table III: List of Important properties of relevant elements [33]

Properties	Ni	Cr	Co	W	Re	Mo	Al	Ti	Ta	Nb	Hf
Melting Point (K)	1728	2180	1768	3695	3459	2896	933.47	1941	3290	2750	2506
Molecular Weight(g/mole)	58.69	51.99	58.93	183.84	186.21	94.96	26.98	47.87	180.95	92.91	178.49
Atomic Radius (pm)	124	128	125	162	137	139	143	147	146	146	159

CMSX-10K has lower creep strain rate among the most of the SX alloys. Figure 3 shows the development of turbine blade alloys which was compared by Lee Langston. The author compared the operating ranges of existing commercial super alloys at a constant creep of 137

MPa. Both CMSX-10K & CMSX-4 has better performances than the other alloys. The properties of CMSX-4 Plus is yet to be determined.

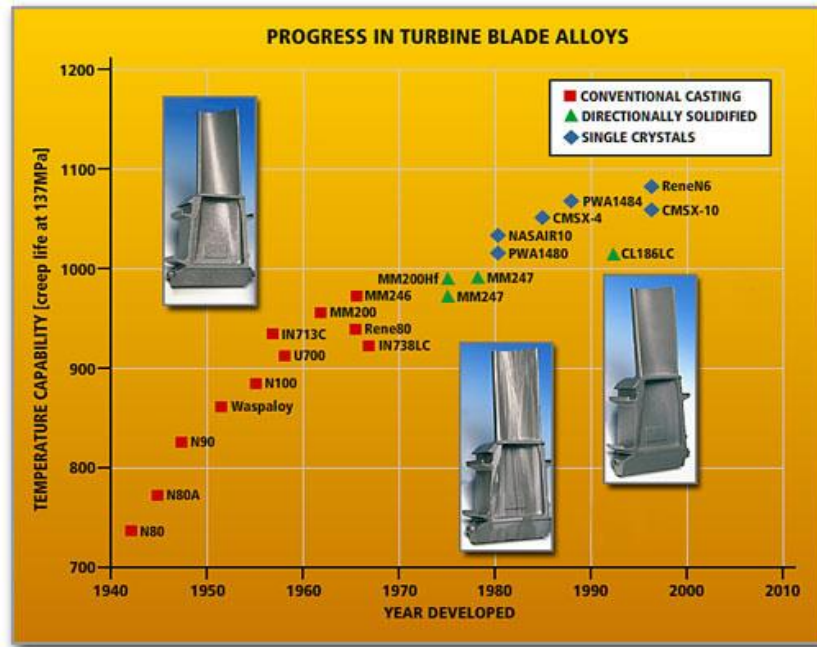


Figure 3: Performance comparison with alloy development [34]

J. Lee and D.M Matson predicted mass evaporation for $Fe_{50}Co_{50}$ using ESL in 2014 [35]. The Authors calculated mass evaporation rate using Langmuir's equation for a two-element alloy system and predicted mass and composition shift with 4.8% and 1.8% error.

This research is an attempt to create a general methodology which will allow researchers to calculate mass evaporation as a function of temperature for complex alloy system. And to do this, the research is subdivided into the following steps to address the questions:

1. To compare ESL and EML sample for CMSX-10 to determine if samples had severe loss of individual element.
2. To identify predictions of mass loss based on test duration calculations (with varying superheat) for CMSX-4+.

3. To conduct ESL experiments to validate evaporation and loss predictions for above test conditions.

3 Methodology

This section explains the methodology and experimental procedure followed for this research.

This research methodology is a modification of J. Lee and D.M Matson's work for evaporation measurement of Fe-Co alloy which has been applied for a complex system of alloy of 11 elements.

3.1 Sample preparation

Single crystal bar of CMSX-4 plus material with 3 in. of diameter and 2.5 in. of height was provided by Canon Muskegon shown in Figure 4. One of the main challenges that we faced during this experiment is to cut the piece of super alloy into desired size and weight. Super alloys are difficult to machine because of their poor thermal conductivity, low modulus of elasticity and strong chemical reaction to tool materials at higher temperatures [36].



Figure 4: Raw material provided by Canon Muskegon

Heat treatment also increases the hardness of Ni based super alloys, so they are difficult to cut.

Our aim was to find a cutting tool which will allow us to cut the metal piece into desired shape

without changing the surface properties and surface quality due to exposure in high temperature. In this context, the combination of water and abrasive machining is an appropriate selection as in conventional machining processes [37], high speed machining requires separate chip removal process and tool life management.

To overcome all these problems, a non-conventional method was used: Abrasive Water Jet Machining (AWJM) which is widely used to cut difficult-to-machine alloys [38]. Pure water jet is used in machining soft metal and to machine our super alloy we needed the help of abrasive material. AWJM is an erosion technique in which water under high pressure and high velocity cuts through the workpiece precisely and grinds away minuscule amount of material. Compared to the other conventional method, the AWJ offers high machining versatility and thermal distortion free sample. The common principle of AWJ cutting is to premix the hard abrasive with water to make a slurry which is forced through the nozzle at a high speed [39]. This is a non-thermal, non-electrical and non-chemical process which creates no change in metallurgical and physical properties of the workpiece.



Figure 5: Abrasive Water Jet Cutter in action in NASA MSFC machine shop

Table IV: AWJ cutting parameters used in machining the sample

Parameters	Units	Conditions
Water Jet Pressure	MPA	280
Traverse Speed	mm/min	40
Standoff distance	mm	2
Abrasive	-	Sand
Abrasive Flow	g/sec	2
Abrasive particle Size	Mesh Size	80
Impact Angle	Degree Celsius	90

This procedure was conducted at the Machine shop of NASA MSFC. Table IV lists the parameter and the cutting conditions used during the cut. The abrasive used for this procedure is a Garnet Red Sand of medium mesh. The abrasive is mixed with the water into a slurry with a ratio of 1:6. The slurry serves several purposes, it carries and distributes the abrasive grains on the work surface. It also cools down the workpieces which avoids thermal stresses. The flow rate of the abrasive was constant. Before cutting, the workpiece was laid carefully on the top of slats which were submerged in the catch tank. The workpiece was kept in a fixed position by two support plates which act like clamps during the cut. Figure 5 shows the AWJM in action. The water jet cuts all the way through the material and the trimmed portion falls of the support plate after the cut. So, to recover the pieces from the water bath was one of the biggest challenge we faced during the procedure. Finally, the cut was made in rectangular shaped with a small portion

joining the pieces which can be seen in Figure 6. Later the smaller pieces were taken out using a hammer.

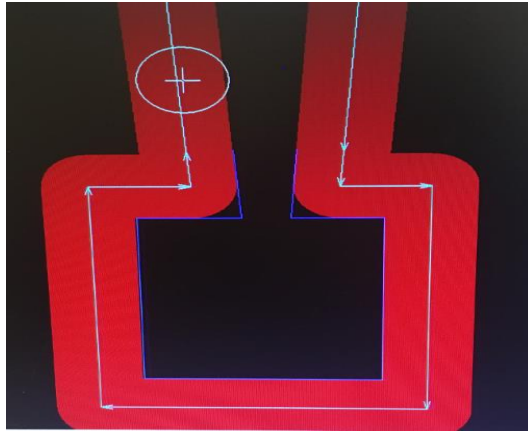


Figure 6: A diagram of the planned cutting path of the sample

After cutting the piece of metal we obtained smaller pieces of width 0.5 cm and height 6.35 cm.

Approximately 6 minutes was taken to cut the bigger piece of the metal into one smaller piece.

Figure 7 shows two small sample rod of 1.91g and 1.71 g obtained using the water Jet cutter.



Figure 7 : Sample rod obtained from AWJ Processing

Next the rod was cut into smaller samples weighing approximately around 60 mg. The water jet cutter could not be used for this procedure, so we needed a precision cutting tool. We used a

medium sized diamond cutting wheel of Model DWH4122 at NASA MSFC facility. Table V lists the properties of the diamond wheel we used during this procedure.

Table V: List of Properties of DWH 4122 Diamond Wheel in NASA MSFC

Properties	Value
Diameter (inches)	4
Thickness (Inches)	0.012
Size	Medium
Concentration	High

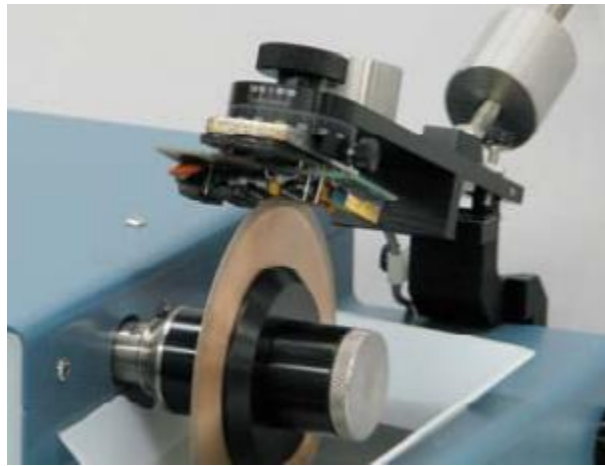


Figure 8 : Diamond Wheel Cutting tool in NASA MSFC ESL facility

The work piece was mounted and fixed between two clamps holding. Grinding is done from only one side of the wheel. The work piece touched the top of the rotating wheel and the specimens were cut perpendicular to the length of the work piece. Figure 8 shows the diamond wheel in action. Ethanol was used as a grinding fluid during this operation which had several purposes. It removed heat and chips and helped in improving grinding wheel life. The samples obtained as small piece into a thickness of 0.05 cm and 0.05 cm. The samples were weighed in precision mass balance to ensure all the samples were in our required range.

Before levitating the sample, we needed to round up the rectangular sample into smoother spherical surface to make it easier to levitate. To get it in desired shape, we arc melted the sample into a temperature range which will not cause drastic amount of evaporation. Electric arc melt furnace can operate up to 1800 degree Celsius which is in the melting temperature range for samples. The pieces were arc melted using a Vacuum Arc Furnace with a water-cooled Copper crucible. A standard Tungsten Inert Gas (TIG) is used as the power source for welding. Heat is generated by the electric arc which struck between the electrode and the sample placed in the crucible melts. In case of making alloys, metals can be melted in electric arc melt furnace to form alloys. Repeated melting improves the alloy homogeneity but for our testing we conducted one melt within carefully regulated temperatures so that we do not have more evaporation the heating was implemented using a heating arc. Figure 9 shown the Electric arc melt furnace in & the sample preparation for arc melt at NASA MSFC ESL facility. Argon was used as an inert gas which do not react with the molten sample. 3.4×10^{-2} Torr of pressure was maintained to prevent impurities and improved homogeneity. The sample processed were weighed with an Electric Mass balance for increased accuracy before and after arc melt. All the samples were weighed in between 30 to 50 mg for levitation purposes.



Figure 9: Electric Arc Melt furnace at NASA MSFC ESL facility

3.2 Experimental Apparatus for ESL

The ESL facility is located at NASA Marshall Space Flight Centre (MSFC) in Huntsville, Alabama. A schematic diagram of the present Ultra High Vacuum Electrostatic levitator is shown in Fig 10. The electrode assembly is housed with all necessary levitation equipment in a cylindrical vacuum chamber. The chamber can be evacuated to an ultimate vacuum of 10^{-8} Torr. Two orthogonal lasers together with two position detectors provide 3D position information to generate a feedback signal. The position sensitive detectors are used for sensing a bright image in a dark background. The sample is backlit by HeNe lasers. A microcomputer converts the detector output to the actual sample position. Figure 11 shows the actual ESL setup located at NASA, MSFC.

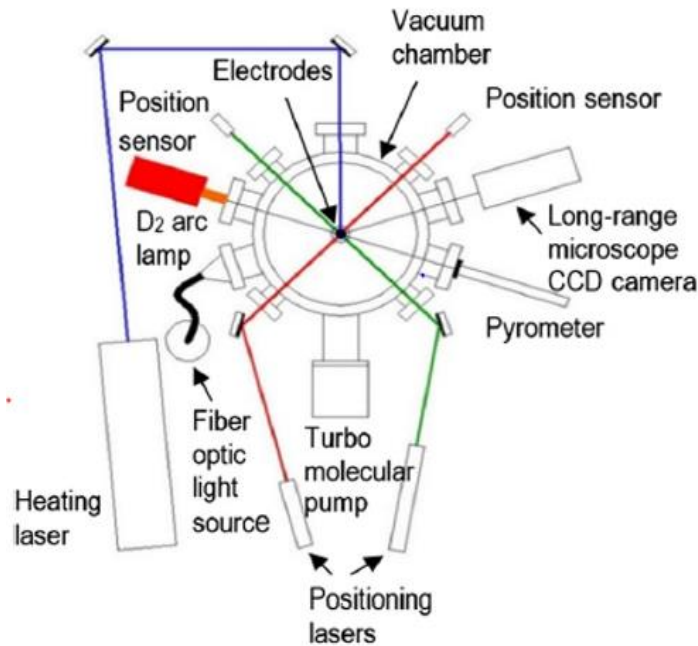


Figure 10: Schematic of the Electro Static Levitator at NASA MSFC [40]

The sample is positively charged and levitated between a pair of top and bottom electrodes which are usually 10 mm apart. An electric field of 8-15 kV/ m is necessary to levitate the typical sample size of 2-3 mm diameter. The sample is heated by a 200 W YAG Laser after

being levitated and stabilized. A custom-built pyrometer is used to measure the sample temperature. The radiative power of a well-defined area of the sample surface into a certain solid angle and over a small wavelength range is collected by the pyrometer. And then through Planck's equation of distribution, the collected power is converted to a sample temperature for the spectral distribution of the emissive power

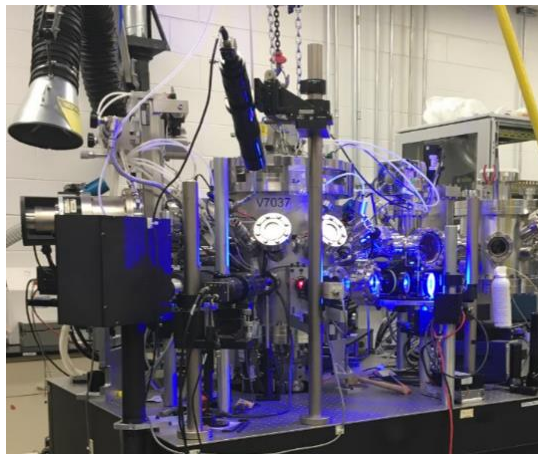


Figure 11: The ESL setup at NASA MSFC (Photo courtesy NASA)

3.3 Experimental Procedure for ESL

The ESL chamber was evacuated to 5.21×10^{-8} Torr by a turbo molecular pump before heating. After the sample was levitated and stabilized by using the electrodes, the sample was heated using the YAG laser. An image of levitated sample during the experiment is shown in Figure 12(a). For tracking mass evaporation, during each thermal cycle the sample was hold at predetermined temperatures for specific times to look into the change in composition. Both pre-processing and post processing mass of the samples were measured for evaporation analysis.

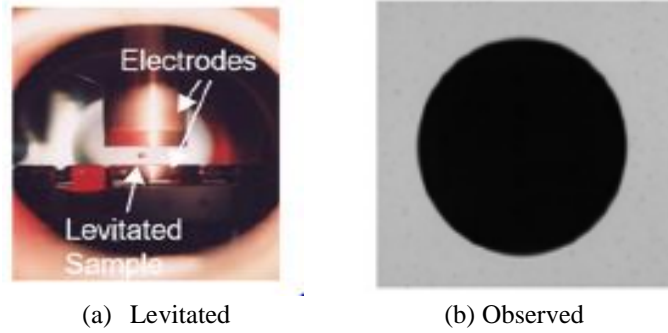


Figure 12: (a) A levitated sample in ESL and (b) a sample observed during density analysis

A WC-Co sphere of 2.2 mm diameter was used for calibration purposes for density analysis. The projected area of the calibration sphere was captured to use as a reference to calculate volume. A high-speed camera was used to capture images of the projected sample between 4 to 8 pixels. After the sample is levitated and heated, the projected shape of the sample is captured by a Redlake High Speed camera of model Y4-S1. The camera captures an image of 512×512 pixels at a rate of 25 frames per second with a resolution of ~0.5microns/pixels. One of the sample image captured during density analysis is shown if Fig 12(b). The temperature of the sample was tracked by an optical pyrometer manufactured by Micron Infrared Inc.

3.4 Electromagnetic Levitation (EML)

This testing is conducted at MSL-EML facility which is controlled out of the Microgravity User Support Centre (MUSC) at DLR-Köln in Germany. In order to reduce preferential evaporation of Chromium, testing is usually conducted in Helium and Argon (~300 millibar). Figure 13 shows the SUPOS coil system which is are used for sample heating and levitation technique. During the experiment, the positioner power is maintained at maximum value to stabilize the sample at the coil center. The cooling rate can be controlled by setting the heater to reduced values.

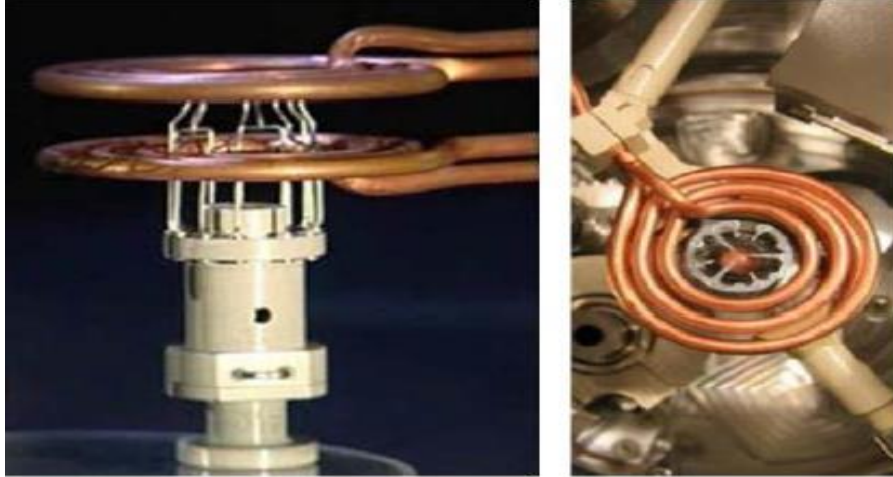


Figure 13: EML SUPOS coil used in positioning and heating sample on the ISS

3.5 Mass Evaporation of Super Alloys

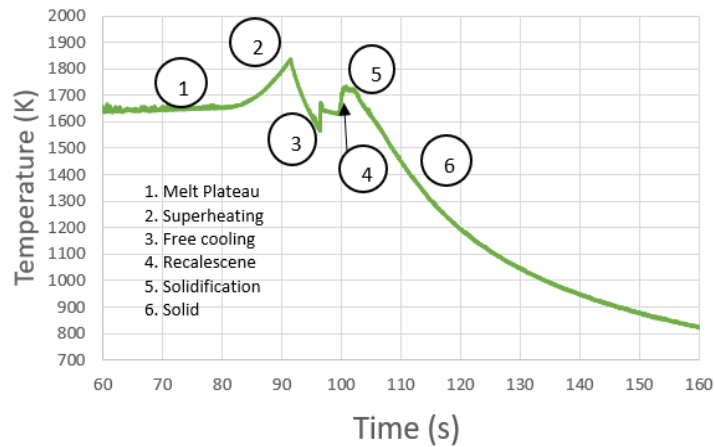


Figure 14: A single melt cycle of one of the CMSX-10 sample

Fig. 14 is a representative of a time- temperature profile of a single melt cycle. The solid sample is heated to its melting point where it remains at constant temperature until its fully melted which is the point (1) in Fig. 3, then the sample is heated at a temperature above its melting temperature point to its superheated temperature (2). After its desired superheated temperature, the heating laser is turned off, the sample cools down freely (3) to its melting point. The sample then

recalesces (4), which is a sudden release of heat due to change in temperature and entropy. The sample then cools down freely to room temperature.

Most samples have impurities as a form of oxides which float on the surface of the sample. Some of the samples were superheated before the actual test so that the oxides can be decomposed to reduce impurities.

The phenomenon of mass evaporation of volatile material can be observed in various metallurgical process. In order to control this process, it is necessary to know the key factors determining its rate including pressure, gaseous atmosphere and the temperature inside the system. The rate of mass evaporation from the surface of the sample to the atmosphere can be calculated using Langmuir's equation for evaporation [41] shown in equation (6).

$$\dot{m} = \frac{\alpha A (P_v - P_{ref})}{\sqrt{2\pi MRT}} \quad (6)$$

Where, \dot{m} is the rate of mass evaporation, α is correction factor, A is surface area of the sample, P_v is the vapor pressure, P_{ref} is the reference pressure, M is molecular weight, R is universal gas constant & T is the reference temperature.

The correction factor (α) indicates the deviation in the rate of mass evaporation compared to the ideal evaporation in vacuum. The correction factor is determined in an iterative process where the difference between predicted mass and actual final mass is determined.

Three more factors are needed to be considered while estimating mass evaporation of alloys. They are:

- (a) Activity of individual components
- (b) Surface segregation
- (c) Final composition

The first factor is the activity of the individual constituents. It is the effective concentration of a species at a specific temperature to its standard state. It is a dimensionless quantity which is dependent on temperature, pressure and composition of the mixture. Usually activity coefficient is used to relate the activity to a measured mass fraction. Activity coefficient (γ) can be expressed as shown in equation (7).

$$\gamma = \frac{a}{c} \quad (7)$$

Where, a is the activity and c is the composition of the substance. Activity co-efficient accounts for deviation from ideal behavior in a mixture of chemical substances. For an ideal solution $\gamma = 1$ and activity is equals to composition.

The total vapor pressure of the alloy is assumed to be the summation of the product of the activity and vapor pressure of the individual components in ideal evaporation according to Raoult's Law [41] for non-volatile solute is equal to the vapor pressure of the pure solvent at that temperature multiplied by its mole fraction as shown in equation (8).

$$P_v = \sum_{i=1}^n a_i P_{v,i} = \sum_{i=1}^n \gamma_i c_i P_{v,i} \quad (8)$$

The rate of mass evaporation of component i in the alloy can be expressed as:

$$m_i = \sum_{i=1}^n \left[\int_0^t \frac{(a_i P_{v,i} - P_{ref}) \alpha_i A_i}{\sqrt{(2\pi M_i RT)}} dt \right] \quad (9)$$

So, the total mass evaporated from the sample is the summation of mass evaporation from each individual alloy element which can be found by integrating the mass evaporation rate with respect to time as per equation (9).

Second factor is surface segregation which can be interpreted using two theories. According to quasi-chemical theory, the constituent having lower heat of vaporization segregates at the surface [43] [44]. The other theory known as the strain theory is based on the atomic size difference of the

constituents [45]. According to this theory, the atoms having the larger size segregate at the surface in order to minimize the strain energy. If there exists larger difference in surface tension between the elements, the component with smaller surface tensions segregates on the surface of the molten sample and evaporates faster. In such case the analysis becomes much more complicated as the diffusion effect of higher surface tension component needs to be considered. Large differences in surface tension combined with lower diffusion results in evaporation of higher surface tension components [46].

The final factor that needed to be considered is change in final composition. Changes in vapor pressure, differences in activity and surface tension throughout the process give rise to compositional shift which needs to be taken into account while calculating rate of mass evaporation. So, the final form of Langmuir's equation to calculate mass evaporation is:

$$m_i = \sum_{i=1}^n \frac{(\gamma_i c_i P_{v,i} - P_{ref}) \alpha_i A_i}{\sqrt{(2\pi M_i RT)}} dt \quad (10)$$

Where, $P_{v,i}$ is a function of temperature.

During the experiment, minor changes to the transmissivity of the optical path or variation in surface condition due to oxidation or surface roughness results in a different liquidus temperature than the actual published value. Pyrometers are sensitive to a specific wavelength and we can get the energy measured by Wien's displacement law at that specific wavelength,

$$I = k \frac{C_1}{\lambda^5} \exp\left(-\frac{C_2}{\lambda T_b}\right) \quad (11)$$

So, the apparent temperature needs to be corrected based on the observed reference temperature.

The theory of pyrometer is relatively simple, it eliminates emissivity by building consistent ratios until certain assumptions true hold.

If T_b is the apparent temperature of the hot body as read by a brightness pyrometer working at a wavelength λ then the emissivity is,

$$\log \epsilon_\lambda = \frac{C_2}{\lambda} \left(\frac{1}{T} - \frac{1}{T_b} \right) \quad (12)$$

where, $\frac{1}{T} - \frac{1}{T_b}$ is the error in pyrometer temperature [47]. At a given emissivity and reference temperature, a second observed signal corresponds to a new temperature, T_L . So, the ratio of signals is:

$$\ln \left(\frac{I}{I_o} \right) = -\frac{C_2}{\lambda} \left(\frac{1}{T} - \frac{1}{T_o} \right) \quad (13)$$

The pyrometer has a pre-programmed value of emissivity and to correct the temperature we just apply a new reference intensity and temperature reading. So, the ratio of intensities at liquidus temperature (T_L) and pyrometer reading temperature (T_p) becomes,

$$\ln \left(\frac{I_p}{I_{pL}} \right) = -\frac{C_2}{\lambda} \left(\frac{1}{T_p} - \frac{1}{T_{pL}} \right) \quad (14)$$

The ratio remains constants for both the pre-programmed temperature conversion basis and new reference temperature basis. We can equate true temperature T, based on measured temperature T_L to the reading of uncorrected pyrometer data T_p based on observed reference T_{pL} ,

$$\frac{1}{T} = \frac{1}{T_p} + \left(\frac{1}{T_L} - \frac{1}{T_{pL}} \right) \quad (15)$$

This method is called Radiance method [47] which yields better result than the linear approximation.

Once the corrected time- temperature profile is obtained, the next step is to express vapor pressure of each individual element as a function of temperature. A lot of equations has been developed to relate vapor pressure to absolute temperature [49] [50] [51]. Vapor Pressure has a

non-linear relationship with temperature according to Clausius-Clapeyron relation [52]. The equilibrium vapor pressure is an indication of liquid's vapor pressure range. To have precise measurement of vapor pressure along the thermal melt cycle it is necessary to express it as a function of temperature. A critical assessment of thermodynamic data has made it to develop a four-termed polynomial equation (16) in temperature which provides vapor pressure of each individual element.

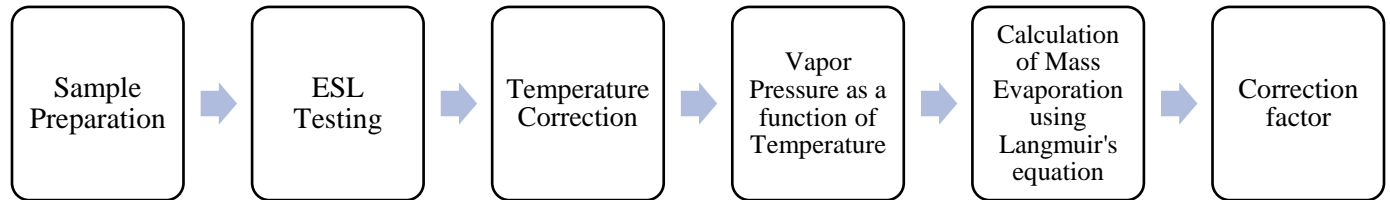
$$\mathbf{Log P_v (atm) = A + B.T^{-1} + C.LogT + D.T.10^{-3}} \quad (16)$$

Table VI: Vapor pressure polynomial equation coefficients for individual element [53]

Element	Temp Range	A	B	C	D
Ni	Sol (298-mp)	10.557	-22606	-0.8717	0
	Liq (mp-2150)	6.666	-20765	0	0
Cr	Sol (298-2000)	6.8	-20733	0.4391	-0.4094
Co	Sol (298-mp)	10.976	-22576	-1.028	0
	Liq (mp-2150)	6.484	-20578	0	0
Mo	Sol (298-2500)	11.529	-34626	-11.1331	0
W	Sol (298-2350)	2.945	-44094	1.3677	0
	Sol (2200-2500)	-54.527	-57687	-12.2231	0
Ta	Sol (298-mp)	16.807	-41346	-0.6735	0
Re	Sol (298-2500)	11.543	-40726	-1.1629	0
Nb	Sol (298-mp)	8.822	-37818	-0.2575	0
Al	Sol (298-mp)	9.459	-17342	-0.7927	0
	Liq (mp-1800)	5.911	-16211	0	0
Ti	Sol (298-mp)	11.925	-24991	-1.3376	0
	Liq (mp-2400)	6.358	-22747	0	0
Hf	Sol (298-mp)	9.445	-32482	-0.6735	0

This equation can be used for ideal gases in the pressure range ($10^{-15} - 10^{-3}$) atm which covers our experimentally accessible range. This four- term precise equation provides data with $\pm 1\%$ accuracy. Table VI lists the required coefficients to calculate vapor pressure using the four-

term polynomial equation. In principal, this equation can be used up to 2500 k temperature which also covers our experimental range. A flow chart of the methodology is shown below:



4 Experimental Results

All the data used for this section has been taken from ESL facility in NASA MSFC and EML facility in German Aerospace Centre (DLR). CMSX-10K data has been tested in both ESL & EML. CMSX-4 Plus has been tested in ESL for different hold temperatures in order to find the compositional change during different melt cycle. Table VII lists the data obtained for CMSX-4 plus from NASA visit in February 2018 for both mass evaporation and density analysis.

Table VII: Data obtained from ESL testing in NASA MSFC for CMSX-4 Plus

Sample	Hold Temperature (K)	Hold time (s)	Pre-arc melt mass(mg)	Post arc melt mass(mg)	Post processing mass (mg)
MAT-1243	Tm	40	39.0264	38.9905	38.8490
MAT-1245	Tm	95	43.9245	43.9081	43.6442
MAT-1246	Tm+50	180	41.6878	41.6777	41.9944
MAT-1247	-	-	46.7895	46.7793	46.5156
MAT-1248	-	-	45.4584	45.4346	45.2987
MAT-1249	-	-	44.6535	44.6334	43.4577
MAT-1250	-	-	40.7758	40.7389	40.4842
MAT-1251	Tm+50	60	41.4308	41.4149	41.0663
MAT-1252	-	-	28.3189	28.3048	-
MAT-1253	Tm-20	80	36.7380	36.7251	36.3851
MAT-1254	-	-	53.6469	53.6352	-
MAT-1255	Tm+100	30	36.3441	36.3291	36.0430
MAT-1256	Tm-20	350	35.6476	35.6271	34.4793
MAT-1257	Tm	250	40.3023	40.5925	40.1125

All of the samples were arc melted before they were processed in ESL. From the table VII we can see a small amount of mass is evaporated during arc melting.

After the experiment is done, data is obtained as pyrometry files database which contains observed pyrometer temperature along with the time elapsed for each thermal cycle. The solidus and liquidus temperature for both samples is listed in Table VIII which indicates there is difference between observed and reference pyrometer temperature. The observed temperature was corrected using Radiance method

Table VIII: Comparison of reference & observed temperature

Material	Reference Solidus Temperature (K)	Reference Liquidus Temperature (K)	Observed Liquidus Temperature (K)
CMSX-10K	1655.15	1706.15	1636
CMSX-4 Plus	1585	1657	1671

Figure 15 shows a time-temperature profile for a single melt cycle of CMSX-10 sample. All samples obtained from both ESL and EML were corrected for temperature using equation (15).

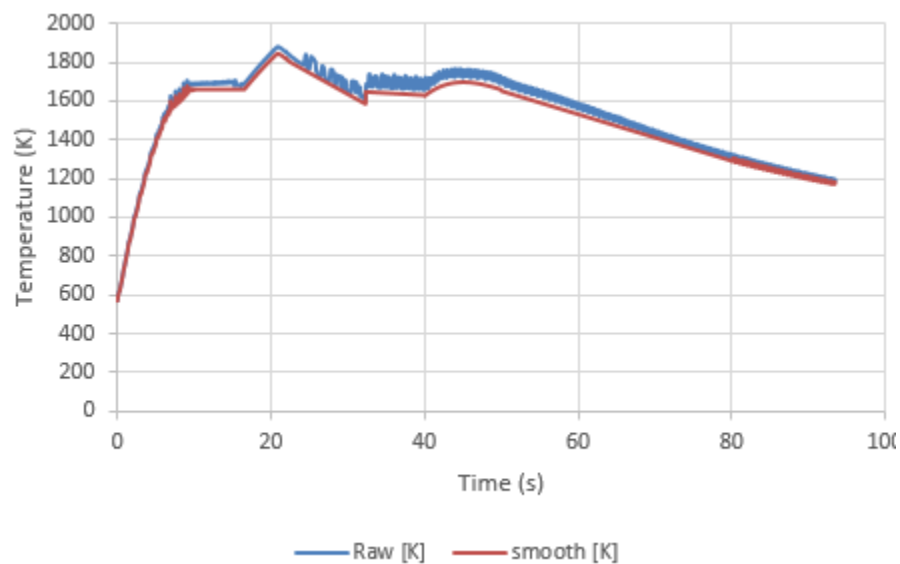


Figure 15: Corrected Time Temperature profile of a CMSX-10K Sample

To measure vapor pressure as a function of temperature for each individual element of the alloys systems, the four-termed polynomial equation (16) and co-efficient from Table (VI) were used. Vapor pressure has been measured and plotted in figure 16 for all the individual elements of CMSX-10K and CMSX-4 plus as Log P (Torr) versus Temperature (K).

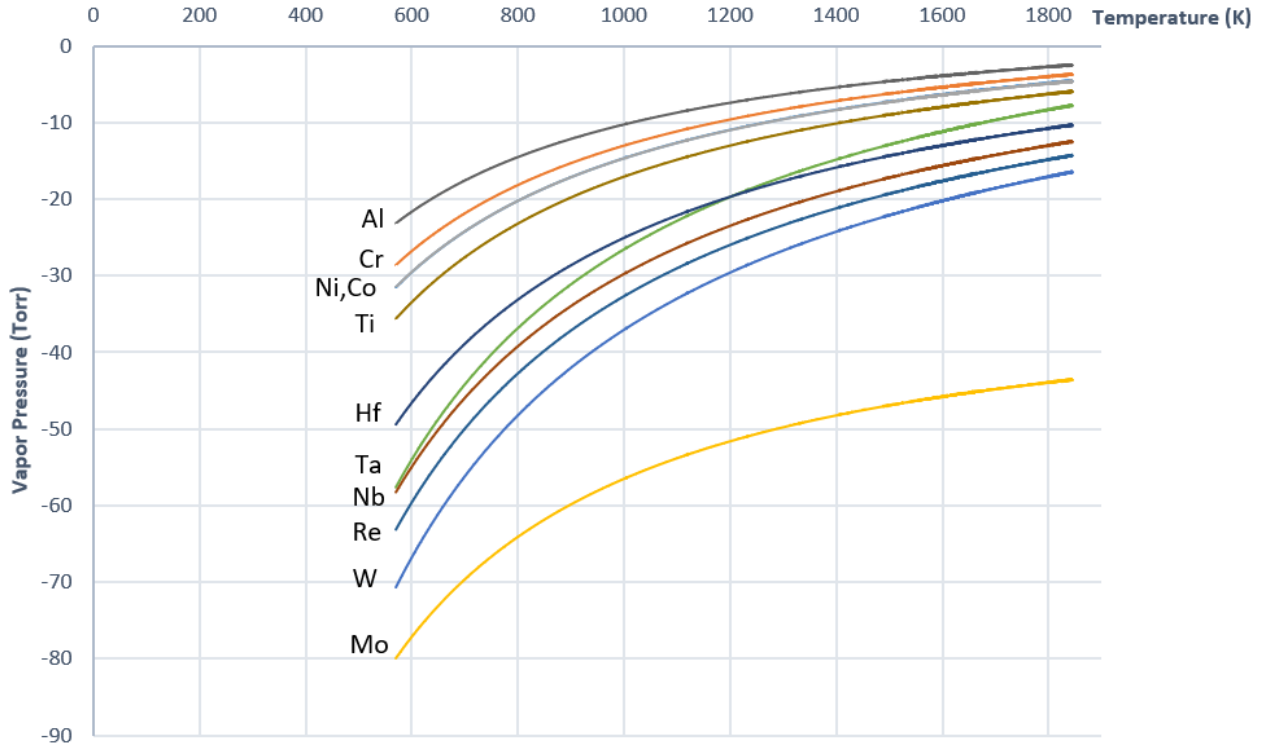


Figure 16: Measured vapor pressure for different element processed in ESL

The density of CMSX-10K has been calculated using the equation (2) & (3) and plotted which can be seen in Figure 17. Since there has been no work on density for CMSX-4 plus we approximated the density using the equations (4) & (5).

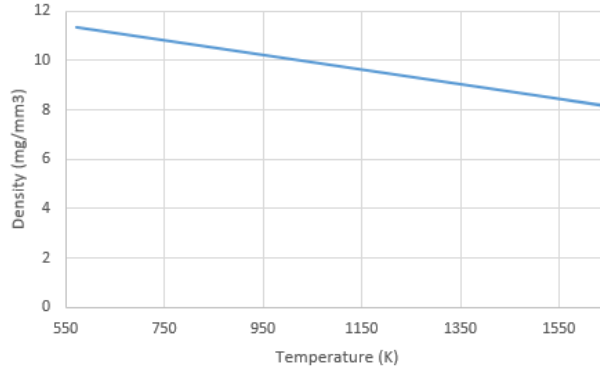


Figure 17: Density of CMSX-10K as a function temperature

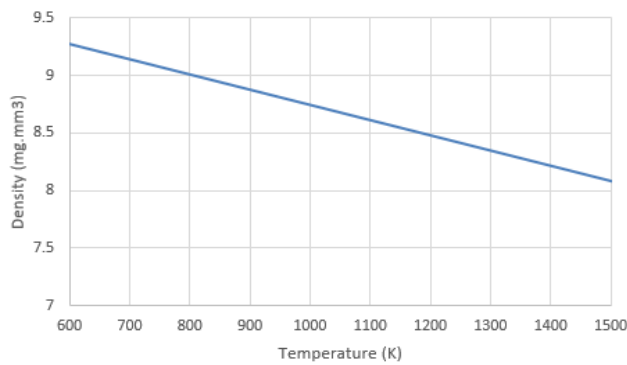


Figure 18: Density of CMSX-4 plus as a function temperature

4.1 Prediction of Mass Evaporation in Ideal Case

To measure mass evaporation for maximum or ideal case the following assumptions were taken:

- Activity co-efficient (γ) equals to 1.
- Correction factor (α) equals to 1.
- Reference pressure (P_{ref}) is zero for ESL & for EML it is 350 mbar.
- Surface segregation is negligible.

Taking all this factors into account, mass loss due to evaporation is calculated using Langmuir's equation for both ESL & EML.

During February, 2018 NASA visit, 14 CMSX-4 plus samples were processed in which 4 of them were tested for density and rest were tested for mass evaporation. After calculating vapor

pressure for all the elements of the corresponding alloy, the data were analyzed to measure mass evaporation by tracking the dynamic mass of the sample over time. In this section, results from two sets of data of CMSX-4 plus processed for two different hold temperatures is discussed. The first one is sample MAT 1256 which has been held at a temperature 20 degree lower than its melting temperature for 350 seconds. The initial mass of the sample was 35.63 mg and the final mass was 34.48 mg. Sample had lots of oxide present on the surface, so the oxides were burned off before holding it at 1620 K. Since the holding process had to be done manually so there is fluctuation of temperature during the hold which can be seen in the time- temperature- mass profile in Figure 19. The ratio of initial mass and final mass of each individual component is calculated and plotted for comparison of mass loss among the elements of the super alloy which is shown in figure 20.

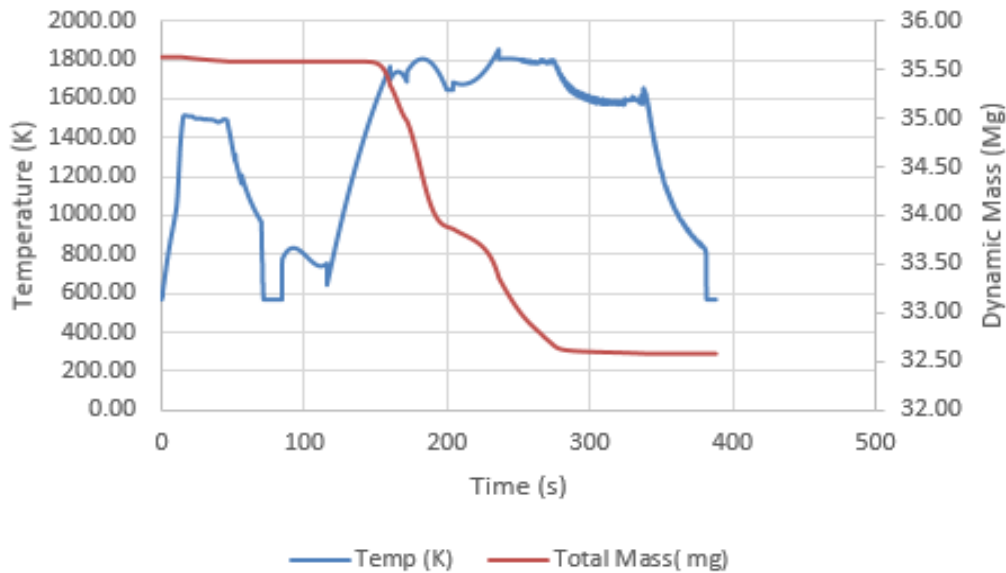


Figure 19: Time-Temperature-Mass profile of a CMSX-4 plus sample MAT 1256

The calculation of dynamic mass for this sample is shown in the following steps:

1. Initial mass of each individual element is obtained from weight composition and its molecular weight. For example, the initial mass of Aluminum(Al) in MAT 1256 is 2.03 mg.
2. The mole fraction can be calculated by dividing the initial mass of the element by its molecular weight. So, the mole fraction of Al is $7.51\text{E-}5$ mole.
3. The density of the material is approximated by the aforementioned equation. The density of the sample at a temperature of 568 K is calculated to be 8.22 mg/mm^3 .
4. The sample resembles a shape of sphere for ESL and using the density calculated in the previous step volume can be obtained which is 4.34 mm^3 for this sample. The radius is 1.01 mm and the surface area of the sample is 1.29 mm^2 .
5. With the corrected temperature from pyrometer, the vapor pressure for each individual element is obtained from the equation (16). For example, the vapor pressure of Al at 1400 K is $2.14\text{E-}4$ Torr. Vapor pressure of all the elements are shown in Figure 14.
6. Taking all the assumptions mentioned into account, the mass evaporation rate for each element is calculated. The mass evaporation rate of Al at 1300 K is $3.64\text{E-}11$ mole/s and the amount of mass loss is $2.18\text{E-}12$ mol.
7. The individual mass loss is combined, and the dynamic mass of its corresponding temperature is obtained. The final mass of this sample is predicted to be of 32.75 mg.

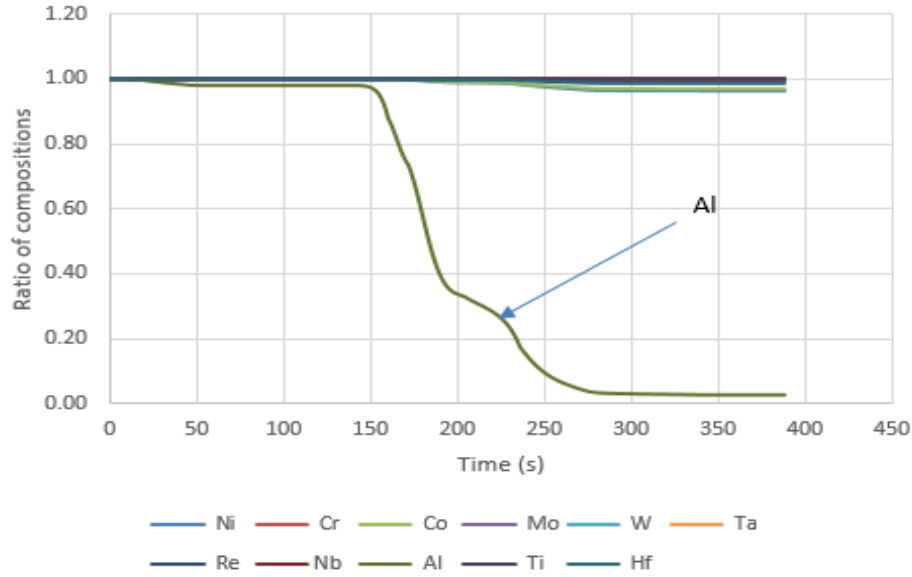


Figure 20: Evaporation comparison of elements of MAT 1256

The second set of data belongs to MAT 1257 which were processed at its melting temperature for 250 seconds. The initial mass of this sample was 40.59 mg and the final mass was 40.11 mg. The model predicts its final mass as 39.2 mg for ideal evaporation. The time temperature mass profile for this sample is shown in Figure 21.

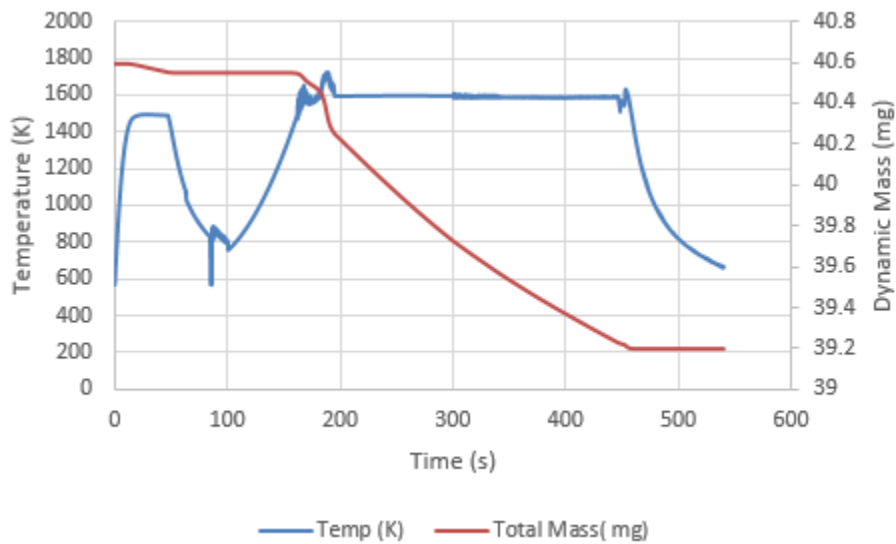


Figure 21: Time Temperature Mass profile of a sample MAT 1257

The oxides were burned off for this sample too and the temperature hold is clearly visible. The ratio of compositions for this sample is shown in Figure 22.

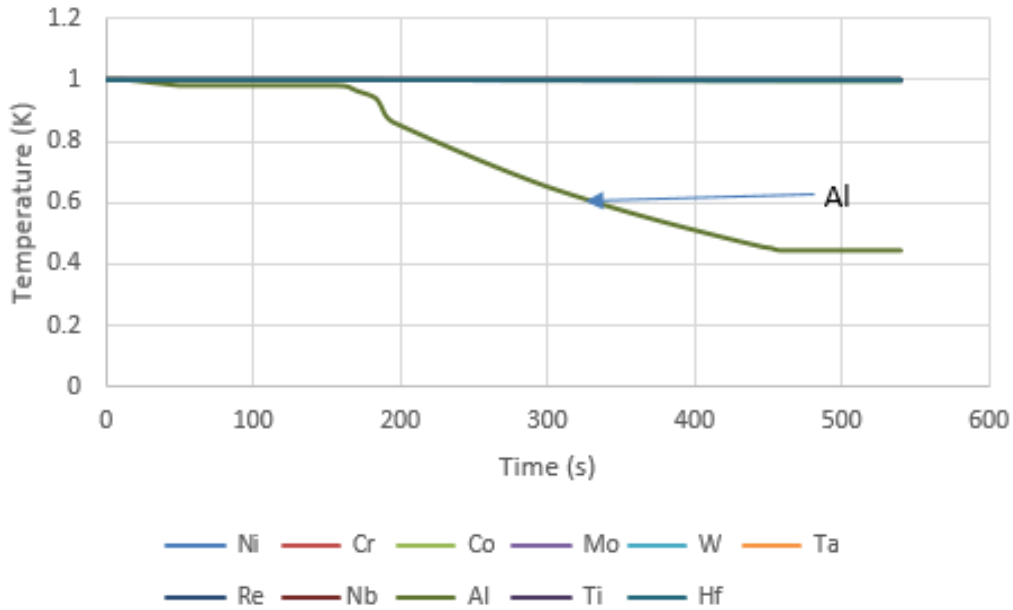


Figure 22: Evaporation comparison of elements of MAT 1257

MAT 867 & MAT 868 both are CMSX-10K sample which were processed using ESL in February 2016. The first sample is processed for 6 melt cycles and for 650 seconds. It has an initial mass of 63.85 mg and 63.40 mg of mass after post processing. The evaporation prediction model was applied to his data and the dynamic mass was calculated by taking into account the evaporation rate of each individual element of the super alloy using Langmuir's equation for ideal case. The model predicts a final mass of 60.25 mg with the mass loss of 3.59 mg for maximum evaporation. Figure 23 shows the time-temperature -mass profile sample MAT 867. The evaporation of volatile element can be expressed as a ratio of initial mass and final mass of each individual element. Figure 24 shows the ratio of compositions for MAT 867 sample.

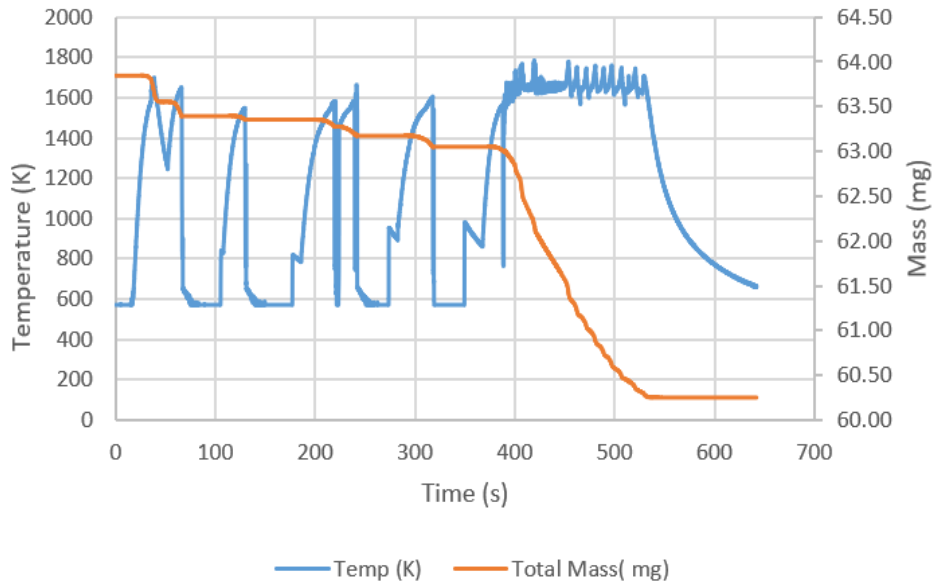


Figure 23: Time-Temperature-Mass profile of a CMS-10K sample MAT 867

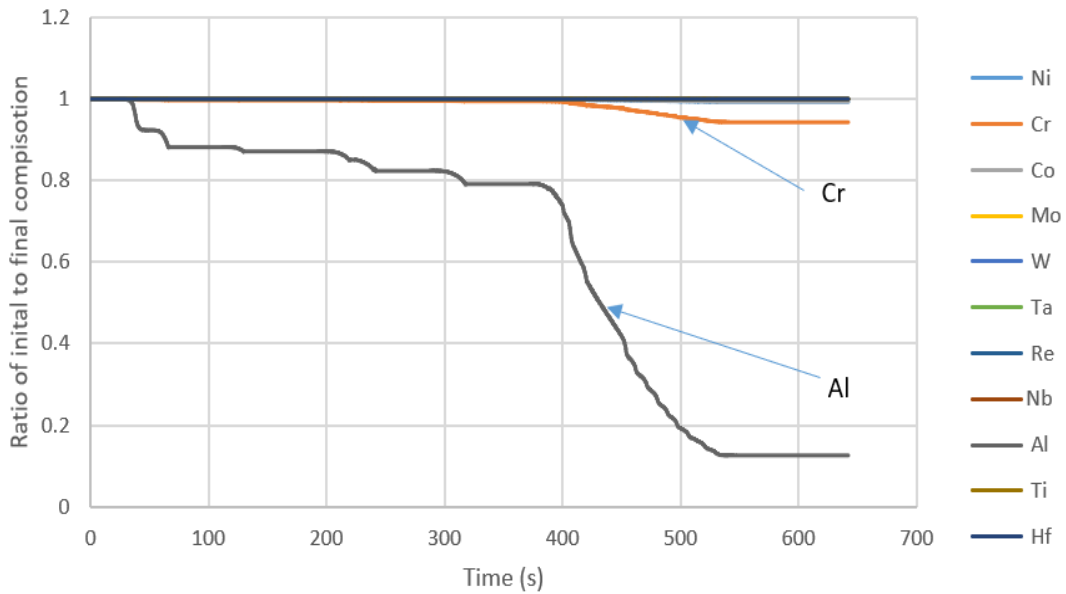


Figure 24: Evaporation comparison of elements of sample 867

The second sample, MAT 868 has been processed with 11 melt cycles for a longer time of 1499 seconds. It has an initial mass of 80.524 mg and final mass of 79.637mg. The model predicts its final mass as 77.39 mg with a mass loss of 3.13 mg. The time temperature profile is shown at

Figure 25. Figure 26 shows the ratio of compositions for the elements of sample MAT 868 as a function of time.

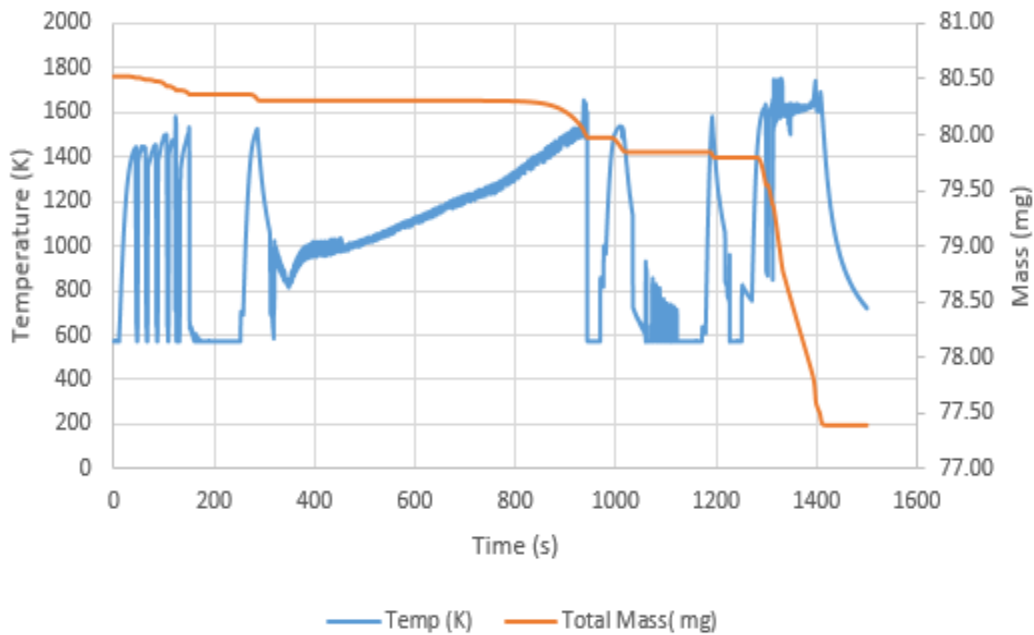


Figure 25: Time temperature mass profile of a CMSX-10K sample MAT 868

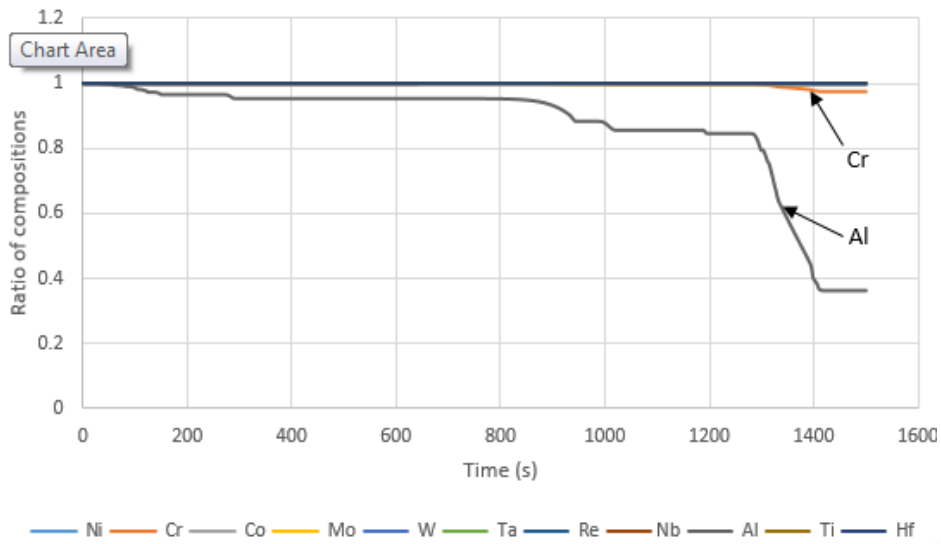


Figure 26: Evaporation comparison of elements of sample 868

After applying this model to ESL data, it has been applied to space data processed at International Space Shuttle (ISS) using Electromagnetic levitation (EML). The processed sample

had a mass of 1000 mg and processed for 22 consecutive thermal cycle. Figure 27 shows the time temperature mass profile of the first melt cycle in EML. The model predicts a mass loss of 967.12 mg and a mass loss of 32.88 mg. And the ratio of compositions is shown in Figure 28.

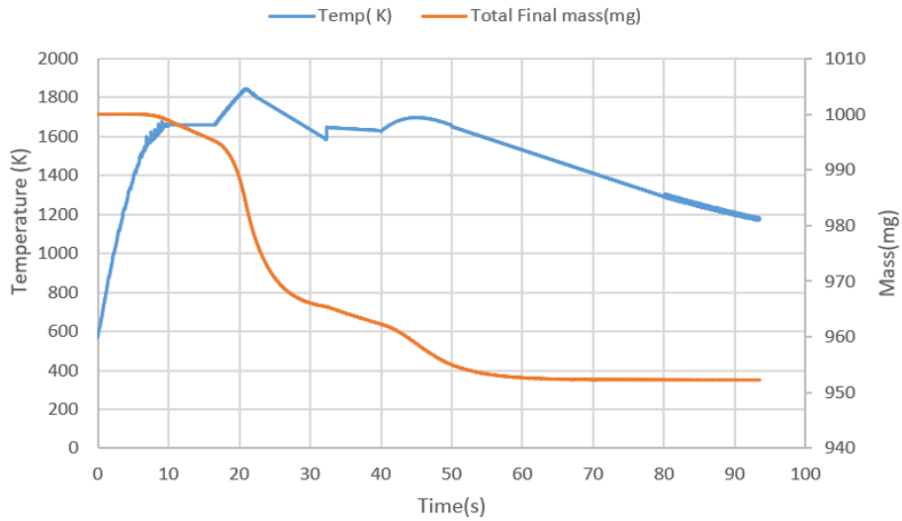


Figure 27: A typical melt cycle of a CMSX-10K sample processed in EML

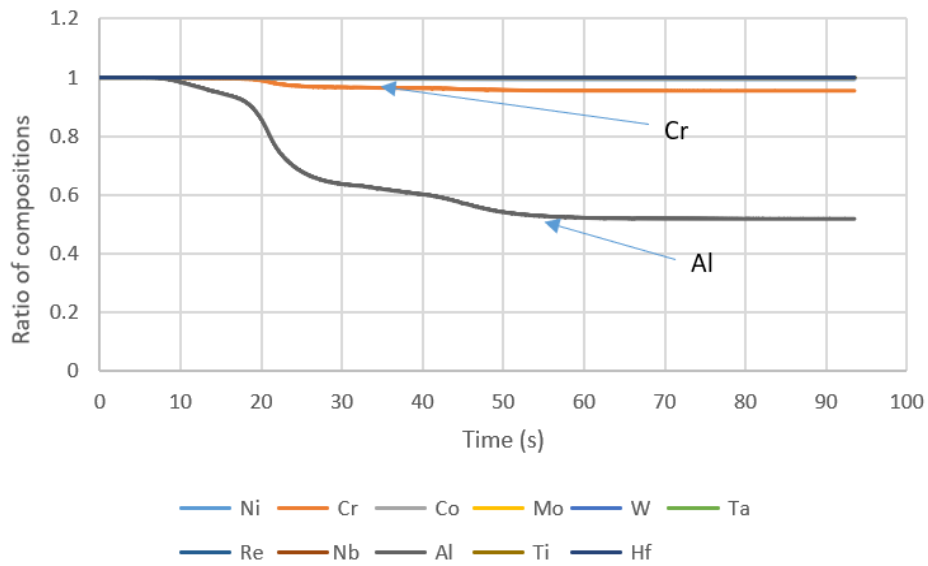


Figure 28: Ratio of compositions of EML sample

This model was applied to all the CMSX-4 plus and CMSX-10 data. A brief overview of Model 1 analysis for three different material is shown in Table IX.

Table IX: Data analysis for Model 1

Material	Sample number	Arc melt mass loss (mg)	Actual mass loss (mg)	Predicted mass loss (mg)	Evaporated element
CMSX-4 Plus (ESL)	MAT 1257	-.29	0.48	1.39	Al (44%) Ni (1%) Cr (1%) Co (1%)
	MAT 1256	0.0575	1.15	2.88	Al (97%) Ni (4%) Cr (1%) Co (1%)
CMSX-10 (ESL)	MAT 867	-	0.45	3.55	Al (42%) Cr (2%)
	MAT 868	-	0.89	0.22	Al (80%) Cr (1%)
CMSX-10 (EML)	SCH_16	-	-	850	Al (100%) Cr (100%) Co (100%), Ti (80%), W (70%)

4.2 Elemental Analysis

After ESL experiment two of the processed sample MAT 1256 & MAT 1257 along with an arc melted unprocessed sample MAT 1254 were sent to Luvak Laboratories, Boylston, MA for elemental analysis. For this elemental analysis Direct Current Plasma Emission Spectroscopy (DCPES) was used. The result from elemental analysis for mass loss is listed in Table X along with the mass loss during arc melt & ESL testing.

Table X: Result from elemental analysis of CMSX-4 plus samples

Element	Initial Composition (%)	MAT-1254 Arc melted (%)	Mat 1256 Processed in ESL (%)	Mat 1257 Processed in ESL (%)
Al	5.69	6.31	5.98	6.04
Co	10	10.2	9.82	9.04
Cr	3.5	3.72	2.34	2.88
Ti	0.86	0.77	0.75	0.69

4.3 Prediction of Mass Evaporation with Corrected Al Activity

From the elemental analysis we can see Al is evaporating with a very small amount. So, another set of calculation was done by assuming no Al is evaporating. Activity of Al was set to zero and a second model was developed. Figure 29 shows the time temperature mass profile for CMSX-4 plus sample 1256. This model predicts evaporation of 0.84 mg against actual evaporation of 1.15 mg. Figure 30 shows the ratio of compositions for sample 1256 for Model 2.

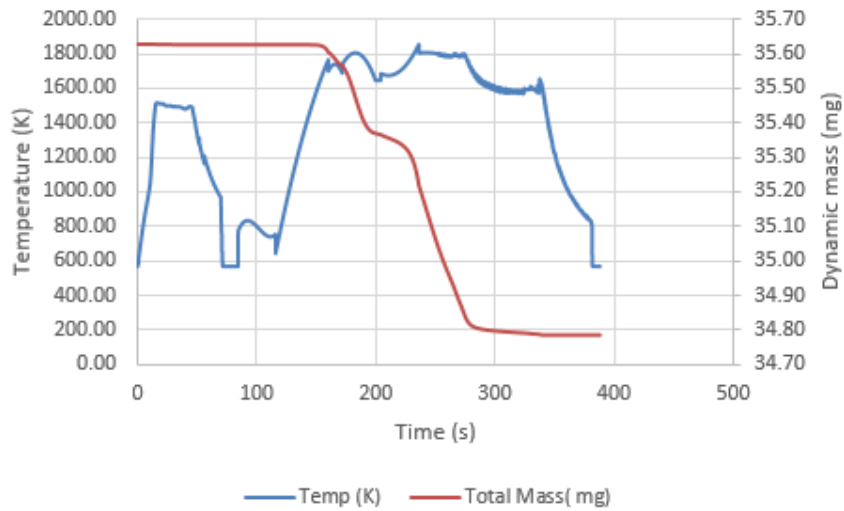


Figure 29: Time Temperature mass profile for MAT 1256 for no Al evaporation

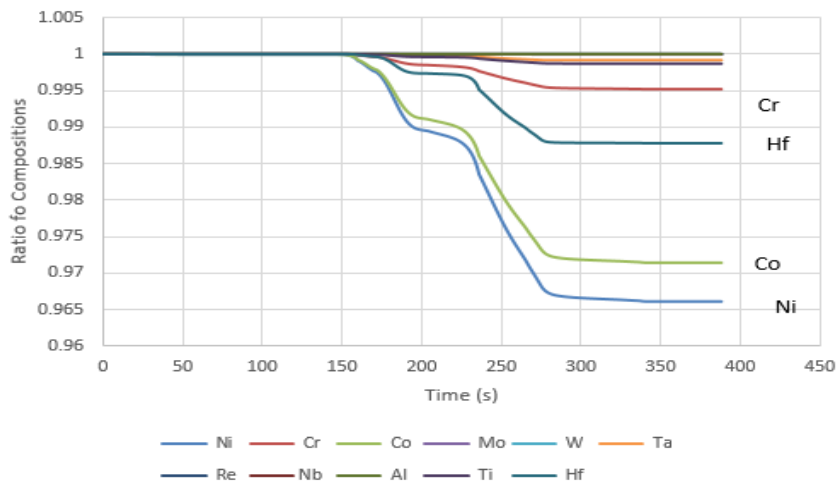


Figure 30: Comparison of compositions while no Al is evaporated in MAT 1256

The model predicts an evaporation of 0.11 mg for actual evaporation of 0.48 mg for MAT 1257. Figure 31 & figure 32 shows the time temperature profile & the comparison of compositions for MAT 1257.

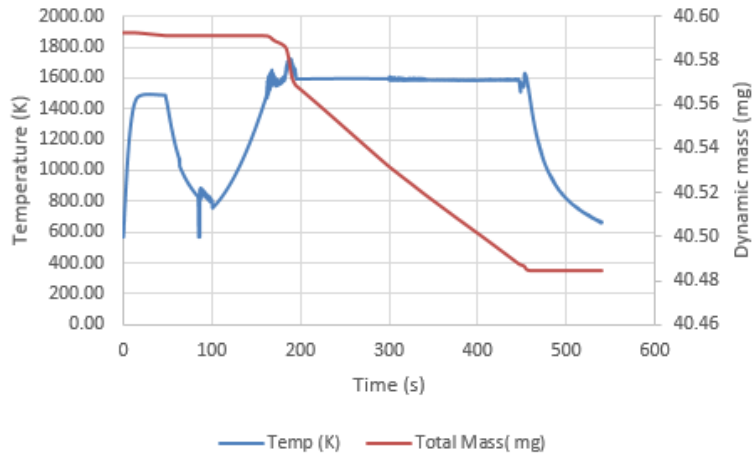


Figure 31: Time temperature mass profile for MAT 1257 for no Al evaporation

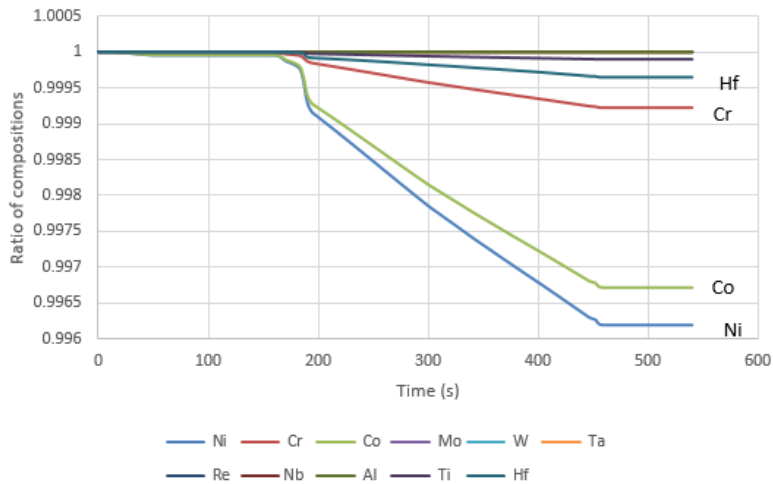


Figure 32: Comparison of compositions while no Al is evaporated in MAT 1257

Same analysis was done for a CMSX-10 sample MAT 867 and the model predicts a final mass of 63.47 as shown in Figure 33. It only has a small amount of Cr & Co evaporated which can be seen in Figure 34.

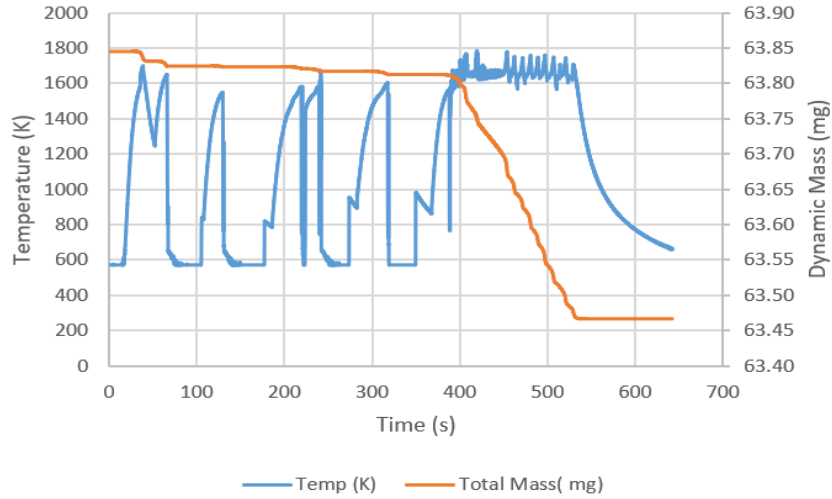


Figure 33: Time temperature mass profile for MAT 867 ($\alpha=0$ for Al)

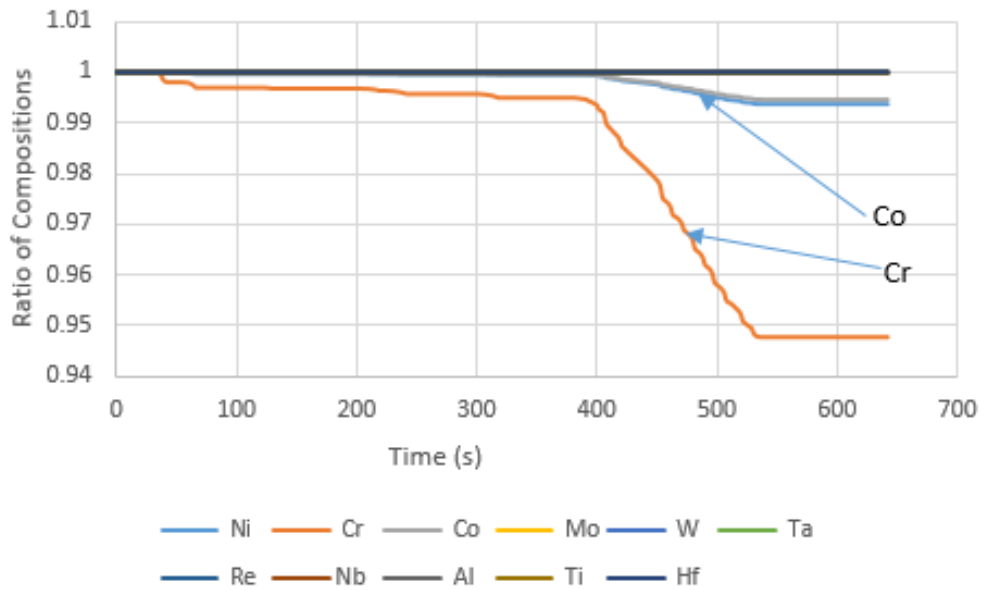


Figure 34: Comparison of compositions while no Al is evaporated in MAT 867

Model 2 was applied for all the samples of CMSX-4 plus & CMSX-10. Table XI shows a brief overview of 5 of the samples and their evaporated elements along with the amount evaporated

Table XI: Data analysis for Model 2

Material	Sample number	Actual mass loss (mg)	Predicted mass loss (mg)	Evaporated element
CMSX-4 Plus (ESL)	MAT 1257	0.48	0.11	Ni (<1%) Cr (<1%) Co (<1%)
	MAT 1256	1.15	0.84	Ni (<1%) Cr (<1%) Co (<1%)
CMSX-10 (ESL)	MAT 867	0.45	0.38	Ni (<1%) Cr (<1%) Co (<1%)
	MAT 868	0.89	0.01	Ni (<1%) Cr (<1%) Co (<1%)
CMSX-10 (EML)	SCH_16	-	550	Ni (<50%) Cr (<45%) Co (<30%) Hf (20%), Ti (44%)

5 Modelling Comparison

This section discusses the errors found in the two models after elemental analysis. The errors were calculated by considering the observed and predicted mass loss of each individual element. The errors were calculated for Al, Cr, Co and Ti. Table XII shows the errors calculated for these elements for both models.

Table XII: Correction Factor & relative error for Three different samples

	Sample 1		Sample 2	
	Model 1 (alpha = 1)	Model 2 (alpha = 0)	Model 1 (alpha = 1)	Model 2 (alpha = 0)
Al	97.29%	2.54%	66.66%	5.54%
Cr	-61.00%	-51.80%	-25.75%	-21.76%
Co	-2.068%	3.75%	-1.10%	2.1%
Ti	-33.33%	-17.39%	-29.06%	-24.96%

Since we do not have the post processed samples from space testing, the elemental analysis was not conducted for EML samples. An overall comparison for mass evaporation of CMSX-4 plus samples are shown in table XIII which lists the evaporation for both models. Standard deviation and mean were calculated for all the samples for better comparison.

Table XIII: Comparison of models for CMSX-4 Plus

Sample	Hold Temperature (K)	Hold Time (s)	Observed Mass Evaporation (mg)	Model 1 Mass Evaporation (mg)	Model 2 Mass Evaporation (mg)	Model 1 deviation	Model 2 deviation
MAT-1243	T _m	40	0.14	0.8	0.059	4.714	-0.579
MAT-1245	T _m	95	0.26	1.33	0.107	4.115	-0.588
MAT-1246	T _m +50	180	0.32	2.36	0.329	6.375	0.028
MAT-1247	-	-	0.26	2.47	0.423	8.500	0.627
MAT-1248	-	-	0.14	0.98	0.08	6.000	-0.429
MAT-1249	-	-	1.18	1.30	0.13	0.102	-0.890
MAT-1250	-	-	0.25	1.92	0.211	6.680	-0.156
MAT-1251	T _m +50	60	0.35	0.38	0.026	0.086	-0.926
MAT-1252	-	-	-	-	-		
MAT-1253	T _m -20	80	0.34	1.19	0.11	2.500	-0.676
MAT-1254	-	-	-	-	-		
MAT-1255	T _m +100	30	0.29	0.69	0.56	1.379	0.931
MAT-1256	T _m -20	350	1.15	2.88	0.84	1.504	-0.270
MAT-1257	T _m	250	0.48	1.39	0.11	1.896	-0.771
Average Deviation						3.654	-0.308
Standard Deviation						2.803	0.586

6 Discussion

The mass loss of the sample is predicted as a function of temperature for corresponding thermal cycle using two different models. The first model predicts mass evaporation for two samples of CMSX4 plus with a factor less than 3. For the two samples of CMSX-10K processed in ESL the model predicts evaporation within 1.5 factors. The CMSX-10K sample processed in EML could not be compared with the actual mass evaporation as the samples are still in space. But the model predicts up to (60-90) % of Al evaporates for all the samples. Very small amount of Cr, Ni, Co, Ti evaporates but these are not significant. The errors in these model ranges from (65-696) % error which is legit as this model predicts the worst-case scenario possible where maximum amount of mass is lost. It can be seen the CMSX-4 Plus sample with lesser hold time but larger temperature shows lesser amount of evaporation compared to the other samples.

The second model is developed by assuming Al does not evaporate at all. In the absence of evaporation of Al, this model predicts the evaporation of other elements of the samples such as Ni, Cr, Co & Hf. The evaporation is insignificant less than 1% for all of these elements.

The elemental analysis from Luvak Inc. shows that weight percentage for Al, Cr, Co & Ti has increased after the arc melt process. Al hardly evaporates along with other three elements. So, a correction factor for Al was applied & the model predicts over all evaporation within $\pm 10\%$ error.

Model 1 predicts evaporation of AL with an error of 97.29 % while for model 2 the error decreases significantly to less than 6 %. For Co model 1 predicts evaporation with an error of -2.06% and for model 2 the error decreases to less than 4 %.

For both Cr & Ti the analysis yielded with significant error. Model predicts evaporation for Cr with an error of -61% and model 2 predicts with an error of 51.80%. For Ti the error for model 1

is less than -34% and for model 2 it is less than 25%. In all the samples surface is segregated for Ti & Cr which results in higher error compared to Al & Co.

The space samples showed significant loss of Al, Cr, Ni, Co for Model 1 after 16 consecutive thermal cycles and for Model 2 the same sample yields loss of Cr, Ni, Co, Hf, Ti, Mo, W up to 50%.

7 Conclusions

This research started with three research questions. After the analysis the answer to those questions are as followed:

RQ1 Yes, the 2nd model predicts mass evaporation within an error of $\pm 5\%$ for actual case.

RQ2 In case of ideal evaporation, most of the Al is evaporating within 200 seconds, 1% Cr & Co also evaporates.

RQ3 For ESL testing even in ideal evaporation no element evaporates within 350 seconds of any samples. So, the testing would be viable for this time frame in ESL. But for space testing in EML the testing is not viable as the model predicts almost 5% of the sample is during on one thermal cycle.

So, the following conclusions can be made through this research:

1. The variation of mass and compositions of CMSX-10K & CMSCX-4 Plus can be estimated using Langmuir's equation of evaporation with negligible surface segregation.
2. Model 1 can be used to predict maximum evaporation rate for super alloys which will yield significant loss of Aluminum.
3. Model 2 predicts mass evaporation with significant reduction in error. This model predicts mass evaporation for Al with error less than 3% and Co with error less than 4%. So, this model can be used to predict mass evaporation for Al and Co.
4. Model 2 predicts mass evaporation for Ti and Cr within 50% of error. So, this model is invalid for predicting mass loss for Ti & Cr.
5. Model 2 predicts mass evaporation with better accuracy than Model 1. The deviation for Model 2 for CMSX-4 plus samples is from -90 to +30 which brackets the zero. So, this model yields error with in a very effective range.

6. Both models for space sample yields significant evaporation so these are invalid for space samples.

8 Future Work

The errors associated with Chromium & Titanium indicates that one of the constituents of the alloy has an activity greater than 1 which is physically impossible. So, for future work we need to run more tests to find out the accurate activity for all the elements.

Correction factor for individual element as a function of temperature will be calculated by taking surface segregation into account. Additional effort will be made to study surface segregation due to the large difference between surface tension of the elements of both super alloys. Systemic under estimation of error has yet to be determined.

More tests need to be conducted to predict mass evaporation for space sample. The diffusion rate and stirring effect in the samples should be accounted for better model development.

Based on the elemental analysis, changes in composition during arc melting needs be considered.

To have better insight on mass evaporation, an overall elemental analysis will be calculated.

More experiments will be conducted to study the effect of mass evaporation in density analysis for newly developed alloy CMSX-4 plus. A correlation between density & temperature will be developed through future studies.

9 References

- [1] B. G. Thomas and L. Zhang, "Mathematical modeling of fluid flow in continuous casting", *ISIJ International* **41**(10)(2001) pp 1181-1193.
- [2] L. Zhang, S. Yang, K. Cai, J. Li, X. Wan, B. G. Thomas, "Investigation of fluid flow and steel cleanliness in the continuous casting strand", *Metallurgical and Materials Transactions B* **38** (1)(2007) pp 63–83.
- [3] Q. Yuan, B. G. Thomas, S. P. Vanka. "Study of transient flow and particle transport in continuous steel caster molds: Part I. Fluid flow." *Metallurgical and Materials Transactions B* **35**(4)(2004) pp 685–702.
- [4] D. Gupta, S. Chakraborty, and A. K. Lahiri, "Asymmetry and continuous casting oscillation of the fluid flow mold: A water model study", *ISIJ International* **37**(7) (1997) pp 654-658.
- [5] S. M. Cho, S. H. Kim and B. G. Thomas, "Transient fluid flow during steady continuous casting of steel slabs: Part I. measurements and modeling of two-phase flow", *ISIJ International* **34**(4) (2015) pp 845–854.
- [6] J. Szekely and R. T. Yadoya, "The physical and mathematical modeling of the flow field in the mold region in continuous casting systems:Part I. model studies with aqueous systems", *Metallurgical and Materials Transactions* **3** (10) (1972) pp 2673-2680.
- [7] I. Egry, A. Diefenbach, W. Dreier, J. Piller. "Containerless processing in space—thermophysical property measurements using electromagnetic levitation", *International Journal of Thermophysics* **22** (2) (2001) pp 569-578.
- [8] T. Ishikawa, P. F. Paradis, T. I. and S. Yoda, "Non-contact thermophysical property measurements of refractory metals using an electrostatic levitator", *Measurement Science and Technology* **16** (2005) pp 443-451.
- [9] D. M. Herlach, "Containerless undercooling and solidification of pure metals", *Annual Review of Materials Science* **21** (1991) pp 23-44.
- [10] S. Mukherjee, Z. Zhou, W. L. Jhonson, W. K. Rhim, "Thermophysical properties of Ni–Nb and Ni–Nb–Sn bulk metallic glass-forming melts by containerless electrostatic levitation processing", *Journal of Non-Crystalline Solids* **37** (1) (2004) pp 21-28.
- [11] M. Langena, T. Hibiya, M. Eguchib, I. Egrya, "Measurement of the density and the thermal expansion coefficient of molten silicon using electromagnetic levitation", *Journal of Crystal Growth* **186** (4) (1998) pp 550-556.
- [12] A. J. Rulison, J. L. Watkins and B. Zambrano, "Electrostatic containerless processing system", *Review of Scientific Instruments* **68** (7)(1987) pp 2856-2863.
- [13] D. M. Herlach, R. F. Cochrane, I. Egry, H. J. Fecht and A. L. Greer, "Containerless processing in the study of metallic melts and their solidification", *International Materials Reviews* **38** (6)(2013) pp 274-347.
- [14] P. N. Quested, R. F. Brooks, L. Chapman, R. Morrell, Y. Youssef & K. C. Mills, "Measurement and estimation of thermophysical properties of Nickel based superalloys", *Materials Science and Technology* **25** (2)(2013) pp 154-162.
- [15] D. M. Matson, R. W. Hyers, T. Volkmann and H. J. Fecht, "Phase selection in the mushy-zone: LODESTARS and ELFSTONE projects", *Journal of Physics: Conference Series* **327** (012009) (2013) pp 1-7.
- [16] D. Y. Kwok, T. Gietzelt, K. Grundke, H.-J. Jacobasch, and A. W. Neumann. "Contact angle measurements and contact angle interpretation. 1. contact angle measurements by

- axisymmetric drop shape analysis and a goniometer sessile drop technique", *American Chemical Society* **13** (10)(1997) pp 2880-2894.
- [17] Y. Sato, T. Nishizuka, K. Hara, T. Yamamura and Y. Waseda, "Density measurement of molten silicon by a pycnometric method", *International Journal of Thermophysics* **21**(6) (2000) pp 1463-1471.
- [18] T. Sugawara, T. Shiono, S. Yoshida, J. Matsuoka, K. Minami, and E. Ochi, "Density measurement of simulated radioactive waste glass by the archimedean immersion method using molten chloride salts", *Physics and Chemistry of Glasses - European Journal of Glass Science and Technology Part B* **54** (9) (2013) pp 270-278.
- [19] A. Pamies, E. Louis and C. Garcia, "The measurement of surface tension of liquid aluminum by means of the maximum bubble pressure method: The effect of surface oxidation", *Scripta Metallurgica*, **18** (9) (1984) pp 869-872.
- [20] W. K. Rhim and K. Ohsaka, "Thermophysical properties measurement of molten silicon by high-temperature electrostatic levitator: density, volume expansion, specific heat capacity, emissivity, surface tension and viscosity", *Journal of Crystal Growth* **208** (1-4)(2000) pp 313-321.
- [21] D. M. Matson, X. Xiao, J. Rodriguez and R. K. Wunderlich, "Preliminary experiments using electro magnetic levitation on the International Space Station", *International Journal of Microgravity Science and Application* **33** (2)(2016) pp 330306.
- [22] W. K. Rhim, S. K. Chung, D. Barber, K. F. Man, G. Gutt, A. Rulison, and R. Erik Spjut, "An electrostatic levitator for high-temperature containerless materials processing in 1-g", *Review of Scientific Instruments* **64** (10)(1993) pp 2961-2970 .
- [23] T. M. Pollock and S. Tin, "Nickel-based superalloys for advanced turbine engines: chemistry, microstructure and properties", *Journal of Propulsion & Power* **22**(2) (2006) pp 361-374.
- [24] N. S. Stoloff, C. T. Liu and S. C. Deevi, "Emerging applications of intermetallics." *Intermetallics* **8** (9-11) (2000) pp 1313-1320.
- [25] S. R. Hegde, "High temperature oxidation behavior of the single crystal superalloy CMSX-10". MS Thesis: *The University of British Columbia*, Vancouver, (2005).
- [26] Z. Yao, C. C. Degnan, M. JEPSON, and R. C. Thomson, "Microstructural and chemical rejuvenation of a Ni-based superalloy", *Metallurgical and Materials Transactions A* **47** (12) (2016) pp 6330-6338.
- [27] F. L. Versnyder and M. E. Shank, "The development of columnar grain and single crystal high temperature materials through directional solidification", *Materials Science and Engineering* **6**(4) (1970) pp 213-247.
- [28] T. M. Pollock and W. H. Murphy, "The breakdown of single-crystal solidification in high refractory Nickel-base alloys", *Metallurgical and Materials Transactions A* **27** (4) (1996) pp 1081-1094.
- [29] P. Caron and T. Khan, "Evolution of Ni-based superalloys for single crystal gas turbine blade applications", *Aerospace Science and Technology* **3**(8),(1998) pp 513-523.
- [30] J. B. Wahl and K. Harris. "CMSX-4 Plus single crystal alloy development , characterization and application development", *The Minerals, Metals & Materials Society* (2016)
- [31] Z. LI, K. C. Millis, M. Mclean, and K. Mukai, "Measurement of the density and surface tension of Ni-based superalloys in the liquid and mushy states", *Metallurgical and Materials Transactions B* **36**(2) (2005) pp 247-254.

- [32] J. Am, "A ready reference of chemical and physical data", *American Chemical Society* **127**(12) (2005) pp 4541-4541.
- [33] E. Ricci, D. Giuranno, R. Novakovic, T. Matsushita, S. Seetharaman, R. Brooks and L. A. Chapman, "Density, surface tension, and viscosity of CMSX-4 Superalloy", *International Journal of Thermophysics* **28** (4) (2007) pp 1304-1321.
- [34] L. Langston and S. Jan, "Gems of turbine efficiency", *ASME, Mechanical Engineering; New York* **136** (9) (2014) pp 76-77.
- [35] J. Lee and D. M. Matson, "Prediction of mass evaporation of Fe50Co50 during measurements of thermophysical properties using an electrostatic levitator", *International Journal of Thermophysics* **35** (9-10)(2014) pp 1697-1704.
- [36] E. O. Ezugwu, "Key improvements in the machining of difficult-to-cut aerospace superalloys", *International Journal of Machine Tools & Manufacture* **45** (12-13) (2005) pp 1353-1367.
- [37] C. H. Lauro, L. C. Brandão, D. Baldo, R. A. Reis and J. P. Davim, "Monitoring and processing signal applied in machining processes – A review", *Measurement* **58** (2014) pp 73-86.
- [38] M. Uthayakumar, M. A. Khan, S. T. Kumaran, A. Slota and Jerzy Zajac, "Machinability of Nickel-based superalloy by abrasive water jet machining", *Materials and Manufacturing Processes* **31** (13) (2007) pp 1733-1739.
- [39] B. Karpuschewski, A. M. Hoogstrate and M. Achtsnick, "Simulation and improvement of the micro abrasive blasting process", *CIRP Annals* **53**(1) (2014) pp 251-254.
- [40] J. Lee, J. E. Rodriguez, R. W. Hyers and D. M. Matson, "Measurement of density of Fe-Co alloys using electrostatic levitation", *Metallurgical and Materials Transactions* **46** (6) (2015) pp 2470-2475.
- [41] J. Lee and D. M. Matson, "Prediction of mass evaporation of Fe50Co50 during measurements of thermophysical properties using an electrostatic levitator", *International Journal of Thermophysics* **35** (9-10)(2014) pp 1697-1704.
- [42] A. L. Myers and J.M Prausnitz, "Thermodynamics of mixed-gas adsorption", *American Institute of Chemical Engineeris* **11** (1) (1965) pp 121-127.
- [43] J. J. Burton and R.S. Polizzotti, "Surface segregation in alloys: dilute solid solutions of Cr, Fe and Ni in Pt", *Surface Science* **66** (1)(1997) pp 1-13.
- [44] J. J. Burton, C. R. Helms, and R. S. Polizzotti, "Surface segregation in alloys: LEED, Auger, and Gas adsorption study of segregation of Au to the surface of Ni", *The Journal of Chemical Physics* **65** ()(1976) pp 1089 .
- [45] F. Weinberg, "Grain boundaries in metals", *Progress in Metal Physics* **8** (7)(1959) pp 105-128.
- [46] T. Lida, "Physical properties of liquid metals : surface tension and electronic transport properties of liquid metals", *Welding International* **8**(10) (1994) pp 766-770.
- [47] C. E. Pyatt, "Some consideration of the errors of brightness and two-colour types of spectral radiation pyrometer", *British Journal of Applied Physics* **5** (7) (1954) pp 264-268.
- [48] S. Briauudeau, M. Sadli, F. Bourson, B. Rougi, A. Rihan and J.-J. Zondy, "Primary radiometry for the mise-en-pratique: The laser-based radiance method applied to a pyrometer." *International Journal of Thermophysics* **32** (2011) pp 2183-2196,.
- [49] A. A. Frost and D. R. Kalkwarf, "A semi-empirical equation for the vapor pressure of liquids as a function of temperature", *The Journals of Chemical Physics* **21** (2) (1953) pp 264-267.

- [50] A. L. Buck, "New equations for computing vapor pressure and enhancement factor", *American Meteorological Society* (1982).
- [51] Y. Waseda, K. T. Jacob, Y. Tsuchiya and S. Tamaki, "Vapour pressure of liquid metals and alloys", *Nature Forsch* **33** (a) (1978) pp 940-945.
- [52] Y. Liu, A. Mahmud, F. Kursawe and T. H. Namb, "Effect of pseudoelastic cycling on the Clausius–Clapeyron relation for stress-induced martensitic transformation in Ni Ti", *Journal of Alloys and Compounds* **449** (2008) pp 82–87.
- [53] C. B. Alcock, V. P. Itkin and M. K. Horrigan. "Vapor pressure equations for the metallic elements: 298-2500K", *Canadian Metallurgical quarterly* **309** (3) (1984) pp 309-313.
- .
- .